A parametric study of the effect of self-oscillating trailing-edge flaplets on aerofoil self-noise

Edward Talboys[a], Thomas F. Geyer[b], Florian Prüfer[b], Christoph Brücker[a]

[a] *City, University of London, London, UK*
[b] *Brandenburg University of Technology, Cottbus, DE*

Abstract

This paper presents an acoustic study of a standard NACA 0012 aerofoil with additional self-oscillating passive flaplets deployed from the trailing edge for self-noise reduction, putting special emphasis on the potential reduction of tonal noise generated by the periodic shedding of vortices from the trailing edge. The flaplets protruding out of the trailing edge act as rectangular thin cantilever beams exited by the surrounding flow to oscillate in their dominant flexural bending mode. The noise attenuation performance is studied for different deployment length, width and inter-spacing to find the most dominant contributions at chord based Reynolds numbers, Re_c from 100,000 to 900,000 and three geometric angles of attack $\alpha_g = 0°, 10°$ and $15°$. It was observed that all flaplet configurations oscillate and thereby reduce the tonal noise. The range of the highest noise reduction in the low frequency range scales with the Strouhal number based on chord length, whereby this range can be set specifically by how far the flaplets protrude out of the trailing edge. This determines the free vibrating length and therefore the natural frequency of the oscillators. Laser-based measurements of the flaplet oscillations confirm the occurrence of a lock-in mechanism observed in previous studies, which effectively describes the oscillating flaplets as pacemaker to keep the fundamental instabilities of the flow in their linear state. It is concluded that this contributes mainly to the tonal noise reduction while the more broadband noise reduction stems from the geometry of the flaplets acting as 'slitted-serrations'. A larger width of the flaplets is most effective in the low-frequency range, while narrower flaplets are best addressing high-frequency noise components. The results further show that a smaller inter-spacing also benefits the noise reduction. The study paves the way for novel morphing techniques to target specific noise ranges during different flight manoeuvres.

Author accepted article submitted to Applied Acoustics *January 21, 2021*

Keywords: Aeroacoustics, Bioinspiration, Self-oscillating flaplets, Aerofoil self-noise

1. Introduction

Engineers have been extensively researching ways to mitigate aerofoil self-noise in recent years. There are various different sources of aerofoil self-noise, as explained in detail by Brooks et al. [1], but the main source of noise is boundary layer – trailing edge interaction. For the current study, laminar boundary layer – trailing edge noise is present and this manifests itself as a strong tonal noise, which is particularly annoying for the human hearing spectrum. As such this tonal noise has had a significant amount of research, to obtain a better understanding of this phenomenon and how it can be avoided.

The first study to investigate in detail tonal noise was carried out by Paterson et al. [2]. They observed that there was an interesting feature, which they named 'laddering', occurring. The main tonal peak frequency was scaling with the freestream velocity, $f \propto U_\infty^{0.8}$, until a certain point when the tonal noise peak made a sudden jump to a high frequency, hence termed laddering. After averaging out all of these laddering events, across a wide range of velocities and frequencies, it was seen that $f \propto U_\infty^{1.5}$. Tam [3] then proposed that the tonal noise is due to an acoustic feedback loop from an aeroacoustic interaction between instabilities in the boundary layer and noise sources situated in the aerofoil wake. The feedback model was expanded by Arbey and Bataille [4], who showed that Tollmien-Schlichting (T-S) waves in the boundary layer diffract at the trailing edge of the aerofoil, subsequently creating acoustic waves that back-scatter upstream, feeding back into the feedback loop. This conclusion initiated more detailed investigations into the flow field around the aerofoil. Lowson et al. [5] and McAlpine et al. [6] first showed that a necessary feature of tonal noise is the presence of a laminar separation bubble on the pressure side of the aerofoil. They then further found that by using linear stability theory, the frequency of the tonal noise component was that of the most amplified instability within the boundary layer. Desquesnes et al. [7] carried out the first direct numerical simulation (DNS) on the tonal noise issue. It was found that there was another, co-existing, feedback loop coming from the instabilities in the boundary layer on the suction side of the aerofoil. It was then thought that this feedback loop modulated the fringe frequencies that are found on either side of the

tonal peak. Pröbsting et al. [8] carried out simultaneous Particle Image Velocimetry (PIV) and acoustic measurements to find that at very low chord based Reynolds numbers (Re_c = 30,000) the tonal noise is generated by the suction side of the aerofoil, while the pressure side dominates the generation of the tonal noise at higher Reynolds numbers (Re_c = 230,000). By tripping either side of the aerofoil separately, it is demonstrated that both feedback loops can exist independently [7]. Arcondoulis et al. [9] built upon this dual feedback loop hypothesis to present an updated feedback model, where the tonal frequency is generated on both sides of the aerofoil. It was observed that these tones have a near exact frequency to each other, but the fringe frequencies were seen to have large differences when comparing either side of the aerofoil. Their experimental observations were then used to develop a new dual feedback prediction model.

Most of the boundary layer – trailing edge mitigation strategies applied by researchers are inspired from the well known 'silent' owl flight. One technique the owl uses, is due to its 'soft downy feather'. These features can be seen as acting like a porous surface, and Geyer et al. [10, 11] investigated the aeroacoustic benefit of having a porous aerofoil. It was found that by even having a small amount of porosity, either by a small streamwise amount of porosity [11] or with a high flow resistivity (low porosity) [10], a benefit can be seen in the low – mid frequency range. As the porosity increases, the benefit increases reaching up 10 dB broadband noise reduction. The benefits do come at a penalty, where there is an increase in high frequency noise. This is primarily due to the increased surface roughness that the aerofoil is then constructed of.

Another owl-inspired technique uses trailing edge brushes or serrations, mimicking the characteristic trailing edge structure formed by the feathers of owls. Herr [12], for which an acoustic reduction was observed in the high frequency range (2–16 kHz). This is believed to be due to the broadband noise of the turbulent boundary layer trailing edge interaction being affected. Finez et al. [13] could show that the spanwise coherence of the shed vortices in the wake behind the trailing edge is reduced by 25% in the presence of brushes.

Serrations have been extensively researched in both the laminar boundary layer case [14, 15] and turbulent boundary layer case [16, 17]. For the laminar case, Chong et al. [14, 15] found that the flat plate extensions were effective at reducing tonal noise by modifying the separation bubble on the pressure side of the NACA 0012 used. Another type of serration that has been sel-

dom studied is slit-serrations. Gruber et al. [18] carried out a comparative experiment on a tripped cambered NACA 651210 aerofoil with saw-tooth serrations and slit serrations. They found that reductions of up to 3 dB can be achieved with the slit serrations at low frequencies but increase the noise level at high frequencies. It was seen that the maximum reduction occurs as the thickness is reduced and the spacing between the slits needs to be small for optimal noise reduction.

Studies with a single flexible flap at the trailing edge were investigated numerically by Schlanderer and Sandberg [19]. They carried out a DNS study on a flat plate with an elastic compliant trailing edge and found an aeroacoustic benefit at low and medium frequencies with an increased noise level at the Eigen frequency of the material. These results were confirmed later by Das et al. [20] in an experimental investigation using a similar arrangement to Schlanderer and Sandberg [19].

The present acoustical study continues a series of original experiments of the authors on arrays of individual self-oscillating elastic elements attached to the trailing edge of an aerofoil to reduce self-noise. This type of trailing edge modification with arrays of elastic flaps has been proven as a novel effective way for passive noise cancellation [21, 22, 23, 24, 25, 26]. This mainly refers to tonal noise, which is generated by the periodic shedding of vortices from the trailing edge of an aerofoil. The noise reduction that can be achieved with the flexible flaplets was attributed to a lock-in process reported in [21], which causes the fundamental instabilities in the flow over the aerofoil - the periodic vortex shedding - to lock-in their frequencies with the natural frequency of the oscillating flaplets. Therefore, these attached oscillators effectively act as pacemaker, keeping the flow instabilities to remain in the state of linear growth. Using high-speed PIV measurements, the authors could show that non-linear instabilities within the shear layer along the suction side were suppressed by adding the flaplets to the trailing edge.

So far, variants of flaplets on aerofoils in these studies focused first on the location to attaching the flaplets to the trailing edge. In Talboys et al. [25], experiments with flaplets tangentially to the pressure and alternatively to the suction sides of a NACA 0012 aerofoil were carried out across a moderate Reynolds number range (50,000 – 350,000, based on chord length). When attached to the pressure side, the flaplets were observed to effectively trip the boundary layer, which, ultimately, had the effect of completely removing the tonal noise component. When the flaplets were on the suction side, it was observed that the tonal noise was significantly reduced due to the

above described lock-in mechanism and the subsequent dampening of T-S instabilities within the boundary layer. All of these effects culminated for the given flaplet geometry and properties in average overall sound pressure level reductions of 3.5, 4 and 2 dB at geometrical angles of attack of $0°, 10°$ and $15°$, respectively.

The objective of the present investigation is to test a broader parameter space of the geometry and properties of flexible trailing edge flaplets to explore the overall noise cancellation potential and the dominant contributions to it. Here the flaplets will be placed inside the aerofoil in a slit along the centre-chord line of the aerofoil, extending with their free ends tangentially out into the flow. By moving the flaps further inwards or outwards of the slit, it is possible to control the free length and therefore the Eigen frequency of the oscillator as they act as one-sided clamped cantilever beams. In addition, the flaplets will be tested at much higher Reynolds numbers than in the previous acoustic study by the authors [25]. The primary focus of the present study is the variation of the flaplet geometrical parameters, such as their length, width and inter-spacing, on the sound power and associated radiated noise. All configurations are tested regarding their acoustic effect in an anechoic wind tunnel facility complemented with detailed velocity measurements in the wake using hot wire anemometry.

2. Experimental Arrangement and Measurement Techniques

2.1. Wind Tunnel

The experiments were carried out in an open jet style wind tunnel at Brandenburg University of Technology, Cottbus [27]. Schematics and a photograph of the set-up are shown in Fig. 1. The wind tunnel was equipped with a circular nozzle with a contraction ratio of 16 and an exit diameter of D=0.2 m. With this nozzle, the maximum flow speed is in the order of 90 m/s. At 50 m/s, the turbulence intensity in front of the nozzle is below 0.1 %. For the present study the chord based Reynolds number (Re_c) was varied from 100,000 – 900,000 and the geometric angle of attack, α_g , was varied from $\alpha_g = 0° - 15°$. The chord used here is the solid aerofoil chord, and as such the length of the flaplets were not taken into account for when calculating the chord based Reynolds number or chord based Strouhal number.

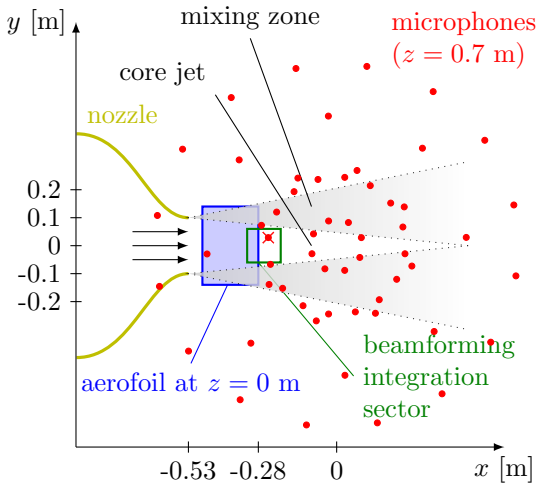

(a) Schematic display of the measurement setup, plan view. The single microphone used is indicated with a red cross.

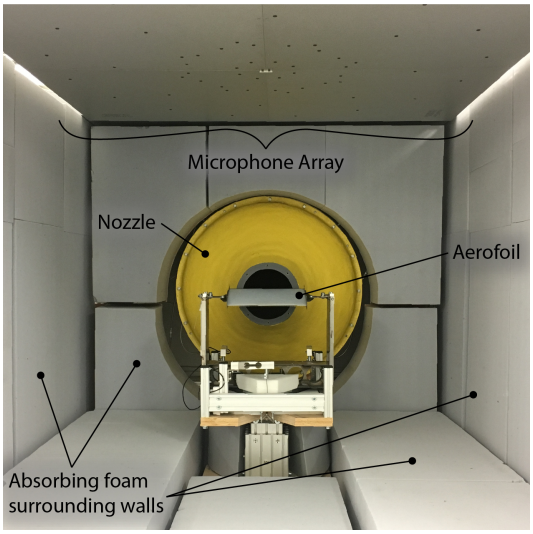

(b) Photograph of experimental set-up, looking from downstream of the aerofoil and nozzle.

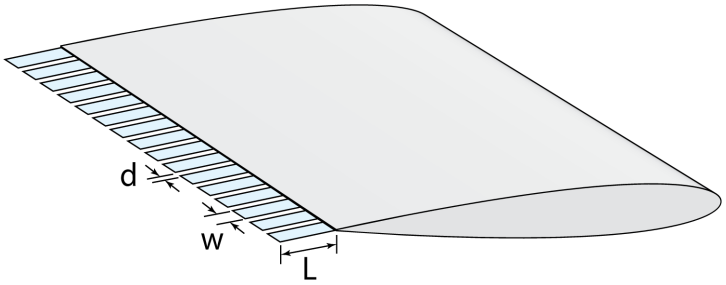

(c) Sketch of the aerofoil with the flaplets attached to the trailing (flaplet spacing d, width w and length L).

Figure 1: Overview of experimental set-up.

2.2. Aerofoil

The aerofoil used is a NACA 0012 symmetric aerofoil, with a chord of 0.19 m and a span of 0.28 m. The span is such that it extends the entire nozzle diameter, to ensure that there are no wing tip effects. The aerofoil was 3D printed, using a polyjet printer, in two halves, where the dividing line was the chord (centre) line of the aerofoil. This allowed the flaplets to be inserted easily along the chord line and extrude out of the trailing edge of the aerofoil, such that the free ends were orientated downstream (see Fig. 1c). This

allows them to freely oscillate at their Eigen frequency (equal to the natural frequency). The determination of the Eigen frequency will be discussed in Section 3.1. The flexible trailing edge flaplets were manufactured, using a laser cutter, from a thin polyester film (see Table 1 for dimensions). It should be noted here that a singular flexible trailing edge, one that spans the entire trailing edge, was not tested in this study. This was motivated by the idea to break-up any spanwise coherence.

2.3. Acoustic Measurements

The acoustic measurements were performed using a planar microphone array consisting of 56 1/4 inch microphone capsules flush mounted into an aluminium plate with dimensions of 1.5 m $\times$ 1.5 m. The array was positioned in a distance of about 0.7 m above the aerofoil (see Fig. 1a). Data from the 56 microphones were recorded with a sampling frequency of 51.2 kHz and a duration of 60 s using a National Instruments 24 Bit multi-channel measurement system. To account for the refraction of sound at the wind tunnel shear layer, a correction method was applied that is based on ray tracing [28]. In post processing, the time signals were transferred to the frequency domain using a Fast Fourier Transformation (Welchs method, [29]), which was done block-wise on Hanning-windowed blocks with a size of 16384 samples and 50% overlap. This lead to a small frequency spacing of only 3.125 Hz. The resulting microphone auto spectra and cross spectra were averaged to yield the cross spectral matrix. This matrix was further processed using the DAMAS beamforming algorithm proposed by Brooks and Humphreys [30], which was applied to a two-dimensional focus grid parallel to the array and aligned with the trailing edge. The grid used has a streamwise extent of 0.7 m, a spanwise extent of 0.4 m and an increment of 0.02 m. The outcome of the beamforming algorithm is a two-dimensional map of noise source contributions from each grid point, a so-called sound map. In order to obtain spectra of the noise generated by the interaction of the boundary layer with the trailing edge of the aerofoil, a sector was defined that only contains the noise source of interest. The chosen sector has a chordwise extent of 0.12 m and a spanwise extent of 0.12 m. Thus, spectra of the noise generated by this mechanism are derived by integrating all noise contributions from within this sector, while all potential background noise sources (such as the wind tunnel nozzle or the aerofoil leading edge) are excluded from the integration. The resulting sound pressures, which represent the values that would be measured at the centre of the microphone array, were then converted to sound pressure

levels, L_p (with a reference value of 20 μPa), and 6 dB were subtracted to account for the reflection of sound at the rigid microphone array plate. It should be noted here that for the 2D sound map figures used herein, a grid increment of 0.01 m was used to obtain better image resolution.

2.4. Constant Temperature Anemometry

Constant Temperature Anemometry (CTA) measurements were taken in separate experiments to the acoustic measurements, to insure no additional noise from the HWA and associated traverse system was measured in the acoustic spectra. The probe used was a Dantec X wire probe (55P64), where the data was taken at a sampling frequency of 25.6 kHz. The Dantec HWA hardware system used for the measurements contains an electronic low-pass filter with a cut-off frequency of 10 kHz. The wake profiles were initiated at $0.25c$ above the aerofoil till $0.25c$ below the aerofoil, at a distance of $0.25c$ from the solid aerofoil edge approximately at mid span. The increment of the measurements was large in the freestream region (1 mm), and then the increment was systematically reduced such that the region of the boundary layer was measured with 0.2 mm increments. Each measurement was taken for a period of 10 s, prior to moving on to the next increment.

2.5. Laser Displacement Measurements

To measure the flaplet displacement within the flow, a laser displacement sensor was used. The sensor used was a Micro Epsilon optoNCDT ILD2300-200, where the frequency was set at $f = 5$ kHz. This was such that sufficient frequency resolution could be obtained to capture the oscillation without sacrificing the quality of the measurements. The sensor was placed beneath the aerofoil such that it was out of the flow of the open-jet. It was positioned in a way that the laser was directed at a point just prior to the tip of the flaplet, so that the true deflection of the tip of the flaplets could be tracked as accurate as possible. Additional care was taken to ensure that the sensor was positioned normal to the flaplets in order to make sure that the back-scattered signal can be accurately detected for signal clarity.

3. Results

3.1. Static Flaplet Response

The Eigen frequency of the flaplets needs to be determined in order to see at what frequency the flaplets will oscillate in the flow. The set-up and

Name	Length (L) [mm]	Width (w) [mm]	Spacing (d) [mm]
Baseline	20	5	1
Long	30	5	1
Short	10	5	1
Wide	20	10	1
Narrow	20	2.5	1
Large Spacing	20	5	7
Medium Spacing	20	5	3

Table 1: Geometric specifications and naming convention for the tested flaplet cases. The thickness of each flaplet configuration was constant at 0.18 mm.

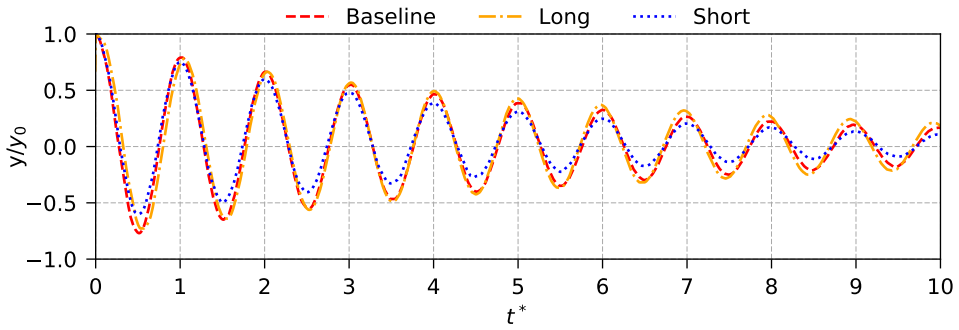

Figure 2: Response of the flaplets to a step input, normalised with the stating position (y_0) and the time is normalised by the measured Eigen frequency ($t^* = t \cdot \omega_n$, t is the time in seconds, ω_n is the observed Eigen frequency in Hz).

image processing for this response test is the same as was used in [21]. The normalised response of the long, baseline and short flaplets is shown in Fig. 2, where $t^* = t \cdot \omega_n$, t is the time in seconds, ω_n is the observed Eigen frequency in Hz, y is the displacement and y_0 is the starting position of the flaplet. Once the Eigen frequency is obtained, the Young's Modulus of the flaplets can be derived using classical cantilever beam theory. Determining the Young's modulus then allows the use of a finite element analysis (FEA) software, in the present case ANSYS, in order to predict the first torsion mode. This is when the flap response enters the flutter regime and therefore provides a limit of frequencies, above which any excitation of this mode may disturb the lock-in effect and add to additional noise. Therefore, the range of tested flow speeds (Reynolds-number) was limited to avoid the excitation of this mode.

From Table 2, each of the flaplets Eigen frequencies can be seen, derived

Case	Experimental	Finite Element Analysis			Estimated
	$f_{1^{st}B}$ [Hz]	$f_{1^{st}B}$ [Hz]	$f_{1^{st}T}$ [Hz]	$f_{2^{nd}B}$ [Hz]	Flutter [Hz]
Baseline	107	110	918	689	455
Long	50	45	547	284	187
Short	345	369	1702	2313	1220
Wide	105	111	494	696	343
Narrow	128	118	1879	740	488
Large S.	104	99	919	620	409
Medium S.	111	110	828	689	455

Table 2: Experimental Eigen frequencies, finite element analysis predictions of the 1st bending ($f_{1^{st}B}$), 1st torsion ($f_{1^{st}T}$) and 2nd bending ($f_{2^{nd}B}$) bending modes and an estimation of the flutter frequency using Eqn. (1) from Xin et al. [31]

both experimentally and by using FEA. It can be observed that there is good agreement between the FEA model and the experiment. As the Eigen frequency is inversely proportional to the squared length, only the short and long flaplets should differ largely in their Eigen frequency. It is important to note that the narrow cases show a higher Eigen frequency than expected. This is assumed to be caused by the laser-cutting process, when additional heat is introduced at the cutting edge. As a result, the Young's modulus of the narrow flaplets was seen to be slightly different to the other flaplets and was adjusted accordingly in the FEA model. When looking at the torsional mode, it can be seen that the long and the wide flaplet cases have a considerably lower torsional frequency in comparison to the other flaplets. Also by looking at the second bending modes, it can also be seen that the long flaplets have a very low second bending frequency. Using the estimated flutter frequency equation given by Xin et al. [31],

$$f_f = f_{n,1} + f_{n,2}/2 \tag{1}$$

where f_f is the estimated flutter frequency, $f_{n,1}$ is the first bending mode and $f_{n,2}$ is the second lowest bending mode (either 2nd bending or 1st torsional mode, whichever is lowest). It can be seen that the predicted flutter frequencies for the long and the wide flaplets are lower than the other configurations and it can therefore be expected that those will go into flutter at a lower Reynolds number, hence limiting the working velocity range for these cases.

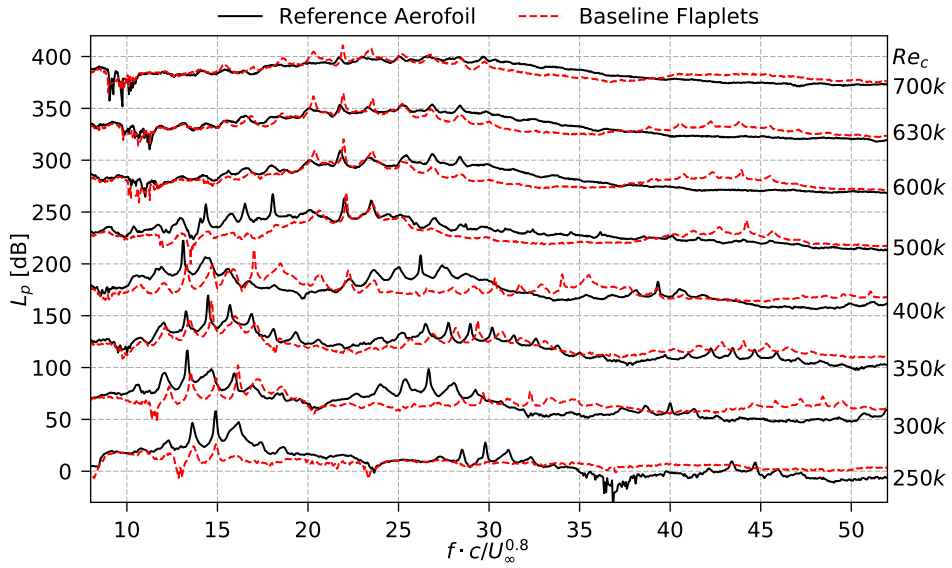

Figure 3: Far field narrow-band sound pressure level spectra re 20μPa for the reference (plain) aerofoil, focusing on the tonal noise produced at $\alpha_g = 10°$. Each of the spectra are spaced with 50 dB from each other for clarity. The frequency has been scaled with the local scaling factor of $U_\infty^{0.8}$.

3.2. Tonal Noise

For the current study tonal noise was seen at all three geometric angles of attack, but for brevity only the results for the reference aerofoil and the aerofoil with baseline flaplets at $\alpha_g = 10°$ are shown here. Figure 3 shows the narrow-band far field acoustic spectra for the chord based Reynolds number where tonal noise was observed, $250,000 \leq Re_c \leq 700,000$. Each of the spectra are spaced with 50 dB from each other for clarity. One of the key features that is observed with tonal noise is distinct frequencies overlaid on a broadband hump. These distinct peaks can be seen in all of the presented cases in Fig. 3. It is well known that as the Re_c is increased, the range of the tonal peaks move to higher frequencies, hence the spectra have been scaled to with the scaling factor proposed by Paterson et al. [2] for local tonal noise. This local scaling is called 'laddering' where this scaling holds true for limited band of Reynolds number prior to jumping to another 'rung'. This can be clearly seen in the spectra obtained for the reference aerofoil, where the frequency of the tonal peaks from $Re_c = 250,000 - 400,000$ increases linearly. To further analyse this effect, Fig. 4 shows the frequency of the tonal

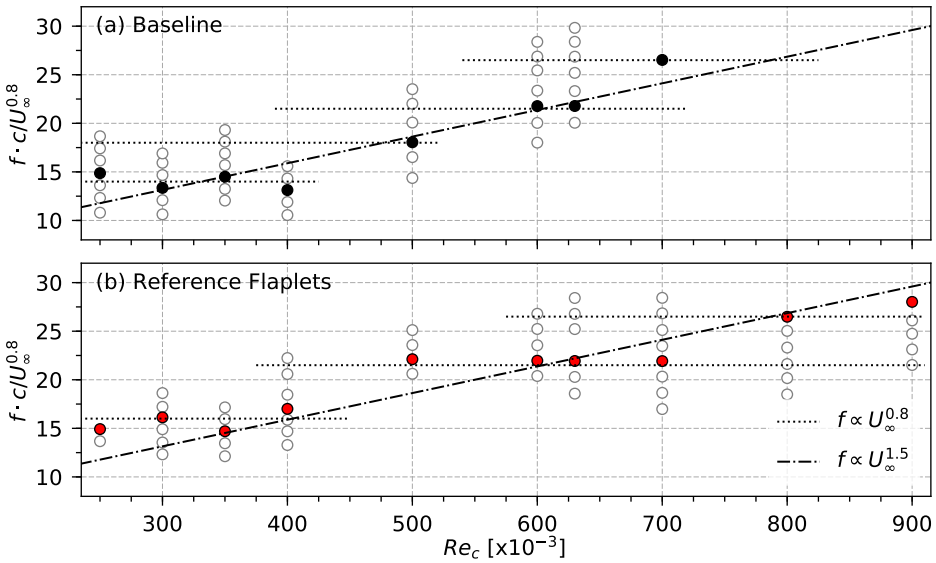

Figure 4: Tonal peaks (solid) and fringe frequencies (hollow) for each Reynolds number at $\alpha_g = 10°$. Global and local trend lines from Paterson et al. [2] are also indicated.

peak and the associated fringe frequencies at each Re_c. The plot includes trend lines both for the local velocity-frequency scaling and for the global velocity-frequency scaling, as proposed by Paterson et al. [2], revealing the typical 'rungs' of the ladder for both the reference and baseline case.

When comparing the reference aerofoil and baseline flaplets tonal noise, it can be seen that the flaplets indeed reduce the magnitude of the tonal noise component, consistent for the whole range of tested Reynolds numbers. In the lowest Re_c case presented, $Re_c = 250,000$, the tonal noise can be seen to be dramatically reduced by the presence of the flaplets, where the tonal peaks are only slightly more pronounced than the low frequency broadband content in the spectra. Furthermore, the tonal peaks extend to a higher velocity than the reference aerofoil due to the presence of the flaplet. In addition, it is visible that the spectra obtained for the reference aerofoil contain a second range of tones at twice the frequency of the first occurrence, which are the first harmonics of the tonal noise. These harmonics are much less distinct in the spectra obtained for the aerofoil with flaplets, especially at low Re_c. These findings strongly indicate that flaplets are dampening the T-S instabilities within the boundary layer. In order to observe this potential damping, a surface oil flow visualisation (SOFV) was carried out at $Re_c = 350,000$ and

at $\alpha_g = 10°$. Figure 5, shows a composite of the SOFV on the pressure side of the aerofoil, with the left side of the image showing the reference aerofoil and the right showing the aerofoil with the baseline flaplets.

The separation bubble can be clearly seen towards the trailing edge of the foil, and either side of the separation the flow is attached. This is due to this area being in the region where the shear layer of the core jet mixes momentum into the flow, keeping it attached. Therefore only the centre part of the aerofoil should be focused on. When comparing the separation bubble, it is immediately clear that the baseline flaplets reduce the separation bubble. The start of the bubble on the reference aerofoil is at $x/c = 0.89$ and the baseline flaplets is at $x/c = 0.87$, showing that the differences that are observed in the spectra are indeed due to the change of the separation bubble on this side of the aerofoil. This delay gives rise to a change in the acoustic feedback loop, hence the probable cause for the slight modification of the frequency that was observed in Fig. 3 and the reduction in the sound pressure level.

In order to enable a better description of the effect of the flaplets on the noise generation compared to the reference aerofoil, far-field noise spectra will be shown in 1/3 octave bands in the remainder of this paper.

3.3. Acoustic,Hot Wire Anemometry and Vibration Results

In this section the results of the 1/3 octave band acoustic spectra, 2D sound maps, overall sound pressure level, hot wire wake measurements and laser displacement measurements will be presented in this order, in turn, for each of the geometric variations, starting with the variation in length, then width and finally the inter-spacing.

3.3.1. Variation in Flaplet Length

Figure 6 shows the acoustic 1/3 octave band spectra at three geometric angles of attack at various chord based Reynolds numbers. In order to visualise all Reynolds number cases on one plot, each spectra are incremented 35 dB from the spectrum at the previous Reynolds number. At $\alpha_g = 0°$, Fig. 6a, a clear tonal noise component is visible for all cases up to a Reynolds number of 250,000. It can be seen that the baseline and long flaplets have little effect on the tonal noise at this angle of attack, whereas the short flaplets show a clear reduction in tonal noise.

What is interesting here is that there is seemingly a strong correlation of length of the flaplets and the frequency range of most efficient noise reduction,

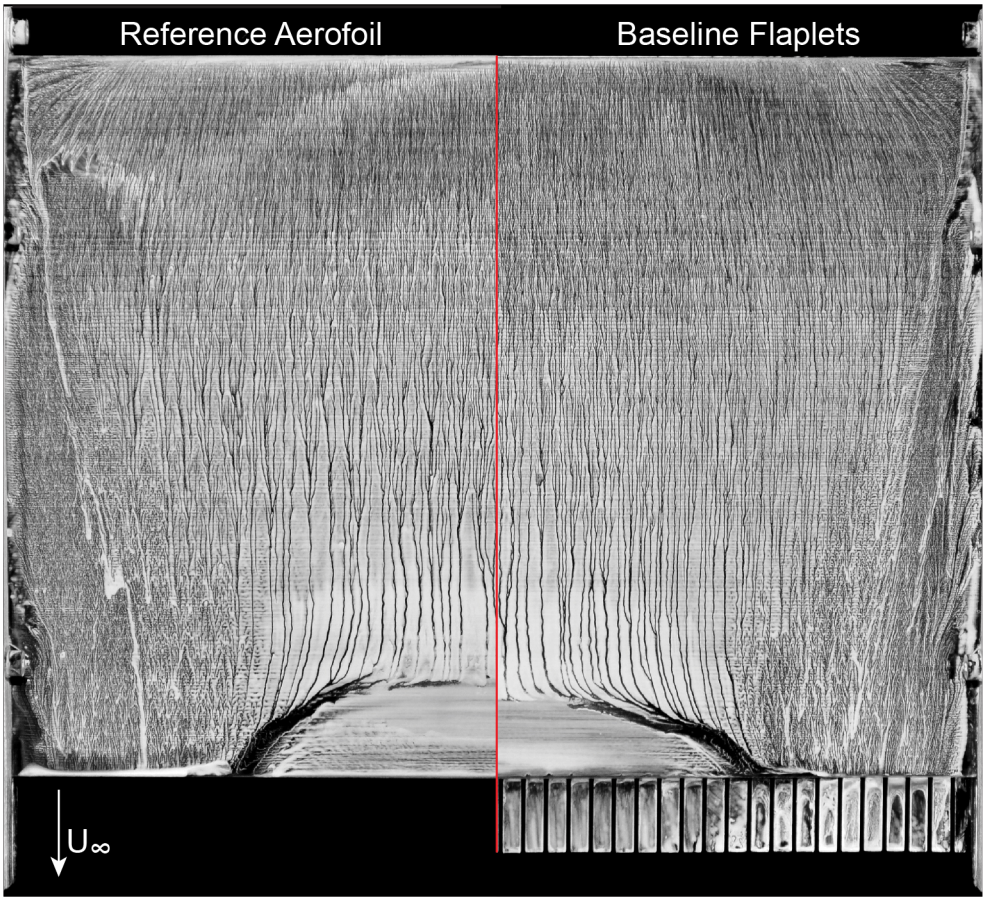

Figure 5: Flow visualisation comparing the pressure side of the aerofoil for the reference aerofoil (left) and the baseline flaplets (right), at $Re_c = 350,000$ and $\alpha_g = 10°$. The flow direction is indicated in the bottom left of the image.

as such it will be discussed separately in Fig. 7.

An interesting feature can be seen at Reynolds number of 600,000, where the long flaplets show a dramatic increase in the noise level, with a peak at $f_c = 200$ Hz. This is when this specific geometry starts to 'flutter'. The flutter is due to the excitation of the lowest two bending/torsion modes of the flaplets. Here it can be seen in Table 2, that the two lowest frequency modes for the long flaplets are the first two bending modes, which leads to a predicted flutter frequency of $f_f = 187$ Hz. This frequency is within the $f_c = 200$ Hz third octave frequency band, showing good agreement with the predicted flutter frequency model from Eqn. (1). This can be observed at the

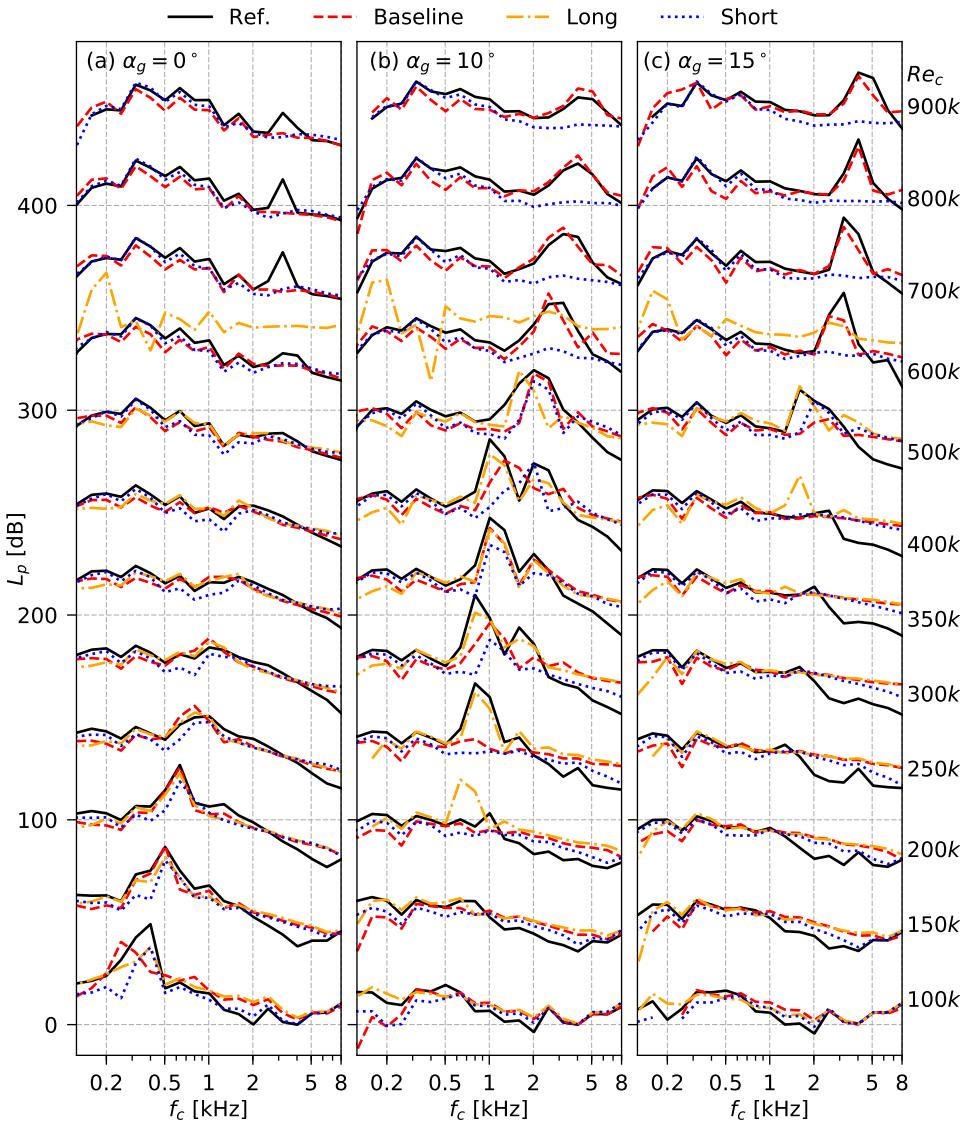

Figure 6: 1/3 Octave band acoustic spectra for variation in flaplet length. Each of the spectra are spaced with 35 dB from each other for clarity.

same Reynolds number for each of the geometric angles of attack, showing that this is indeed the critical Reynolds number, where the flutter is excited for this geometry. It can also be seen that all of the flaplets increase the noise level at frequencies above 5 kHz. Again, as at low frequencies, there

is a distinct order in which the noise level is increased. The most elevated levels are observed for the long flaplets, while the least comes from the short ones. At a Reynolds number of 700,000, there is an emergence of trailing-edge bluntness noise at approximately 3 kHz on the reference aerofoil. As is to be expected, the flaplets reduce/remove this noise component, as they are effectively reducing the bluntness from $\approx$ 1 mm to the thickness of the flaplets (0.19 mm).

As the angle is increased to $\alpha_g = 10°$ (Fig. 6b), the emergence of tonal noise can be seen at a Reynolds number of 250,000 for the baseline case, and is present up to the highest Reynolds number tested (900,000), as previously discussed in Section 3.2. A similar trend as for the zero degree angle case is observed: All the flaplets show a reduction in the low frequency range and an increase at the higher frequency range, the magnitude of this modification being tendentiously higher.

The tonal noise component is in general reduced at all flaplet cases, albeit that the long flaplets only show a small reduction in comparison to the reference. Saying this, at $Re_c = 600{,}000$ and above the baseline flaplets are approximately at parity with the reference case and, interestingly, the tonal noise is completely removed for the short flaplets. The longest flaplets are seen to enable the initiation of tonal noise even before the reference case. This is believed to be due to the flaplets, at this Eigen frequency, promoting the formation of the separation on the pressure side of the aerofoil, the necessary mechanism for tonal noise.

At the highest tested angle, $\alpha_g = 15°$, the tonal noise on the reference aerofoil starts to occur at higher Reynolds numbers. This is consistent with previous literature [25]. All the trends that have been observed at $\alpha_g = 10°$ can also be seen at the increased angle. Again, the magnitude of the effects are increased further.

To quantify the low frequency noise reduction, Figure 7 shows the ΔL_p contours using single microphone measurements, where the microphone used is indicated in Fig. 1a for reference. The columns show the different flaplet geometries and the rows are indicating the different geometric angles of attack. Looking at the first column, for the baseline flaplets, clear zones of noise reduction and noise increase can be determined. The reduction zone can be identified by using limits of chord based Strouhal number, with the lower limit being $St_c = 0.6$ and the upper limit being $St_c = 4$. As the angle increases, the lower limit slightly increases to $St_c = 0.9$, whereas the upper limit stays the same. The magnitude of the reduction can be seen to be the

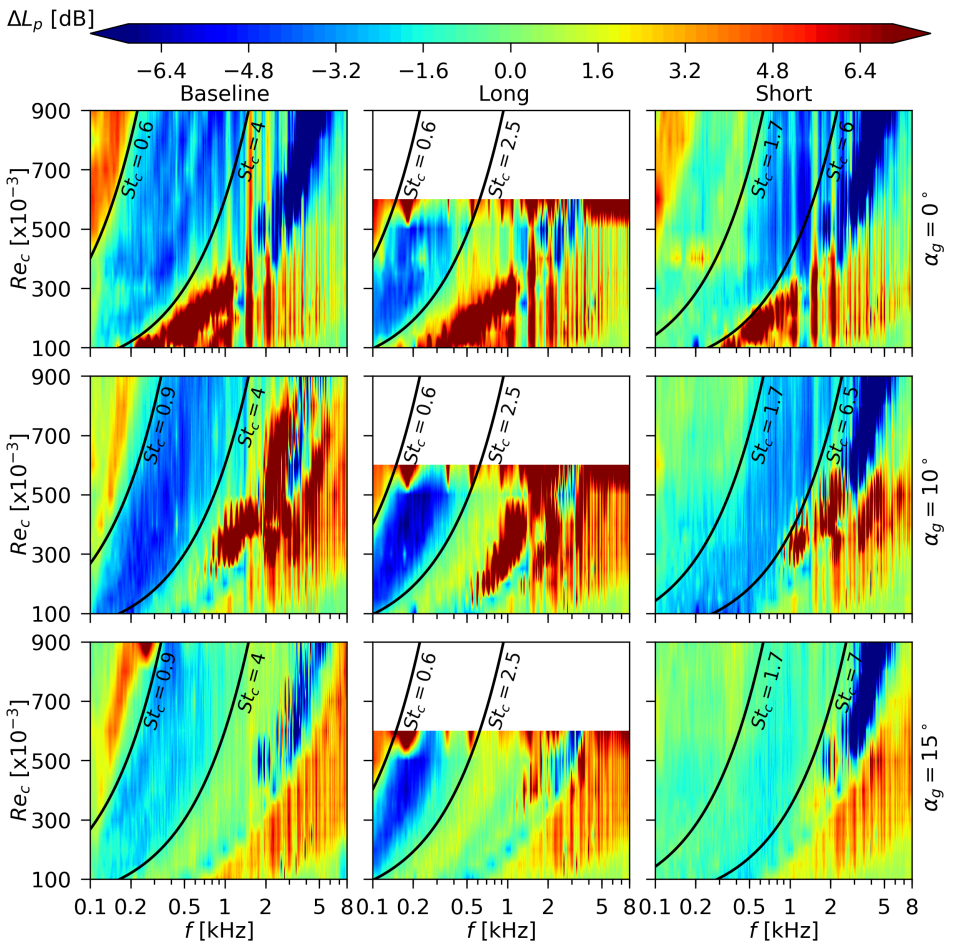

Figure 7: ΔL_p contours for variation in length, with the zone of maximum reduction indicated.

most at $\alpha_g = 10°$. Increasing the angle further, shows the reduction zone is still there however the magnitude of the reduction is reduced. Beyond these reduction zones at $\alpha_g = 0°$ and $10°$, it can be seen that there are regions of high noise increase. This high noise is due to the tonal noise effects caused by the shift in the tonal noise frequency by the flaplets, hence a seemingly large noise increase. This effect can be seen for all flaplets at these angles. When the flaplets length is increased, the bounds of the reduction zone can be seen to have reduced, where the maximum limit is $St_c = 2.5$. This means that a lower band of frequencies can be reduced. As was seen in the base-

line case, the magnitude of reduction was seen to increase at $\alpha_g = 10°$ and then slightly reduce at $\alpha_g = 15°$. Here we should remind the reader, that at $Re_c = 600,000$ the long flaplets went into resonance, hence the spectra for Re_c greater than this are not available for this contour. Finally the short flaplets, again cause a change to the reduction zone, where the bounds have increased to $St_c = 6 - 7$ depending on the α_g. It should be noted that due to the tonal noise component these bands could be different if there were no tonal noise component (i.e. just turbulent boundary layer noise) but investigating this is out of scope of this publication and is left as future work. Also there is a strong reduction at high Reynolds numbers and high frequencies, this is due to the trailing edge bluntness noise reduction as was discussed in Fig. 6. As was previously mentioned in the discussion of Fig. 6, the magnitudes of the reductions also seems to differ with the different flaplet length. It can be clearly seen that the long flaps at $\alpha_g = 10°$, show significant reduction in this low frequency band with a maximum reduction of up to 8 dB and an average of approximately 5 dB, whereas the baseline flaplets show reductions of approximately 4 dB. The shortest flaplets show the least reduction, within this low frequency zone, where the average reduction is approximately 3 dB.

The mechanism of this reduction is not totally clear and should be investigated in further detail with the use of simultaneous particle image velocimetry and acoustic measurements. However the authors have two concepts of thought on the source of the reduction. The first is the hypothesis of the lock-in effect documented in [21] (flaplets act as pacemaker), which plays an important role in the stabilisation of the T-S waves. Because of the different Eigen frequencies of the flaplets, they are modifying the wake with different frequencies, hence the different acoustic frequency reductions. This type of vortex shedding noise reduction has also been observed by Geyer et al. [24], where they used a cylinder with flexible flaplets on the aft part of the cylinder.

The other hypothesis is that it is due to the shape of the flaplet geometry, where the flaplets are effectively 'slit-trailing edge serrations'. A somewhat similar low frequency noise reduction was observed by Gruber et al. [18] with cardboard slit serrations, both experimentally and analytically. However the analytical approach was able to determine multiple frequencies that could be reduced, whereas their experimental results only really showed one reduction zone, similar to the results herein. We should note here that, small vibrations from the cardboard-type serrations cannot be excluded in their experiments in a similar fashion as the flaplets herein. As the observed effect is already

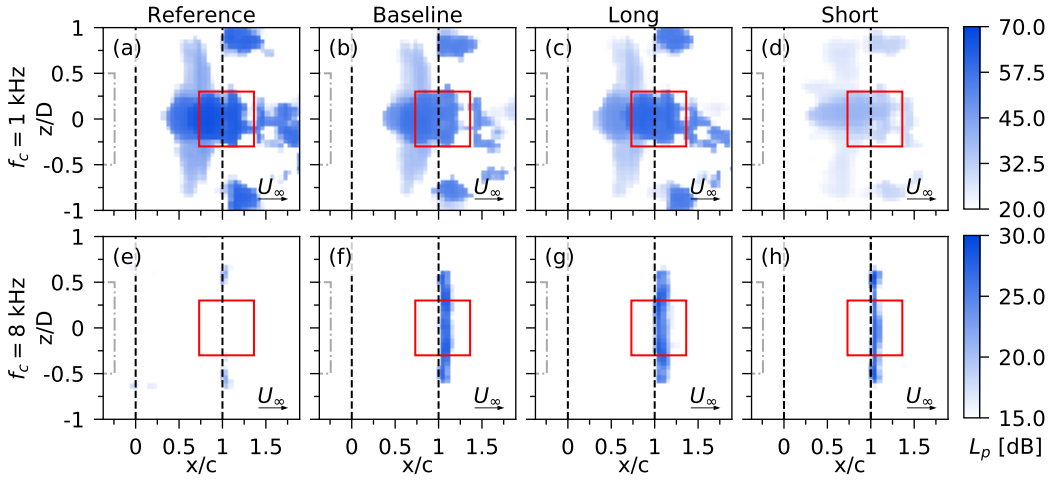

Figure 8: 2D sound maps as the flaplet length is varied, at Re_c=350,000 and $\alpha_g = 10°$. (a–d) shows the frequency band, f_c=1 kHz and (e–h) shows the frequency band, f_c = 8 kHz. (- · - · -) indicates the jet nozzle, (- - -) indicates the aerofoil, (——) indicates the interrogation region for acoustic spectra.

visible for vibration amplitudes as small as 100-200 μm. Furthermore, their noise reduction was focusing on the broadband noise while the flaplets herein clearly address the tonal noise components. So, a definite conclusion cannot be drawn, rather we assume that both mechanisms are involved in the overall noise attenuation effect.

In order to view the location of the dominant acoustic sources, sound maps can be used. These maps are shown as sound pressure levels on a discretised grid that can be interrogated to observe certain noise sources in certain frequencies bands. These sound maps are presented as plan views of the test set-up, and in each of the plots the nozzle exit, leading and trailing edge and the spectral integration zone are indicated.

Figure 8 shows such 2D sound maps obtained at Re_c = 350,000 and $\alpha_g = 10°$ for the frequency bands with centre frequencies f_c of 1 kHz and 8 kHz respectively. This specific testing condition has been chosen as a clear tonal peak can be seen in the acoustic spectra for the reference case, which therefore forms a good basis to compare any tonal noise reduction.

Tonal noise has been previously shown to be reduced with the presence of flaplets. From Fig. 8a it can be seen that the noise source starts from the chordwise position x/c $\approx$ 0.3 extending beyond the solid trailing edge and is located in the mid-span location of the aerofoil. It must be noted here

that there are small regions of increased noise at either side of this large noise source. These noise sources are due to the interaction of the shear layer of the wind tunnel, which is highly turbulent, with the trailing edge of the aerofoil. Looking at all the flaplet cases it can be seen that with the baseline and long flaplets (Fig. 8b-c) there is only a small reduction of the tonal noise, whereas, in contrast, the short flaplets (d) reduce the tonal noise significantly.

When investigating the locations of the acoustic sources with respect to the observed high frequency noise increase, the sound maps at a 1/3 octave band with $f_c = 8$ kHz are better suited than those obtained at 1 kHz. As seen in Fig. 8e, at the higher frequency the reference case now only shows noise sources where the jet shear layer interacts with the leading edge and trailing edge of the aerofoil. It can then be seen for the flaplet cases that somewhat weaker noise sources appear directly aft of the solid trailing edge and along the length of the flaplets, which correspond to the increase in noise levels seen in the acoustic spectra in Fig. 6. This is thought to be due to the oscillatory motion of the flaplets giving rise to an additional acoustic source. It can be seen that this source is a function of the flaplets surface area, as there is a clear difference in the extension of the source from the trailing edge as the flaplets increase in length. Where (h), corresponding to the short flaplets, is the smallest region and the largest area is seen in (g) which is for the long flaplets.

As a means to investigate the overall acoustic effect of the flaplets, the overall sound pressure level (OSPL) has been computed for each of the cases according to

$$L_{pt} = 10\ \log_{10}\Big(\sum_{f_c=0.2\ \text{kHz}}^{8\ \text{kHz}} 10^{\frac{L_{pi}}{10\ \text{dB}}}\Big)\ \ \text{dB}, \tag{2}$$

where L_{pi} is the sound pressure level at the i^{th} centre frequency (f_c). In order to obtain an easier appreciation of the magnitude of the differences between the cases, the difference between the reference case and the different flaplets cases has also been calculated as

$$\Delta L_{pt} = L_{pt,\text{flaplet}} - L_{pt,\text{reference}}. \tag{3}$$

The results are shown in Figs. 9a-c-e.

At $\alpha_g = 0°$, Fig. 9a, it can be seen that as the Reynolds number increases, the general trend is that the OSPL also increases. There is a slight reduction in OSPL from Re_c= 200,000 – 250,000, which is due to the tonal noise component being reduced at this condition. When comparing the flaplet cases

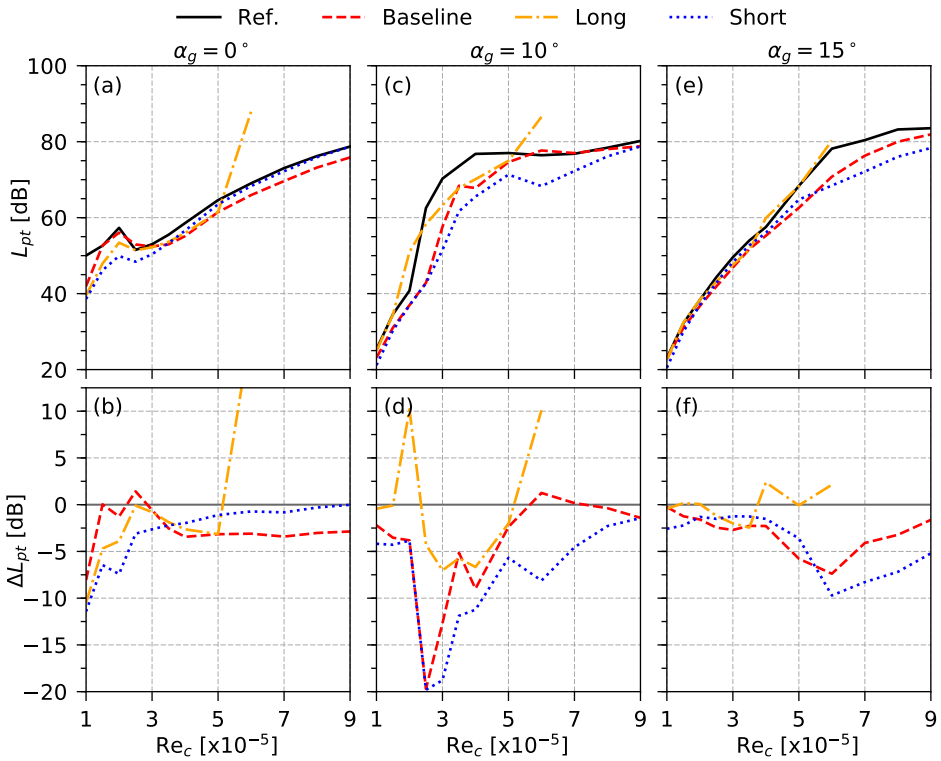

Figure 9: OSPL, denoted as L_{pt}, and Delta OSPL, ΔL_{pt}, for variation in flaplet length.

to the reference case, Fig. 9b, it can be seen that at the lowest Reynolds numbers up to 350,000, the shortest flaplets show the best overall reduction. This reduction is of the order of 5 to 10 dB. After this point the OSPL of the shortest flaps tends back to the reference case. The OSPL for the baseline flaplets, on the other hand, is initially approximately the same as that for the reference case and then tends to a reduction of ∼3.5 dB from a Reynolds number of 400,000 onward. The long flaplets show reasonable overall reductions at low Reynolds number until the sudden noise increase occurs at Reynolds numbers above 500,000, as can be seen in the acoustic spectra. At $\alpha_g = 10°$, Fig. 9c, the reference case leads to a sudden increase in OSPL at Re_c= 250,000. This is due to the prevalent tonal noise that dominates the spectra. Once the Reynolds number reaches 400,000, the OSPL plateaus for the remaining tested Reynolds numbers. Immediately it can be seen that for the baseline and short flaplet cases, the OSPL is lower across the whole range of Reynolds numbers. The largest reduction of approximately 20 dB

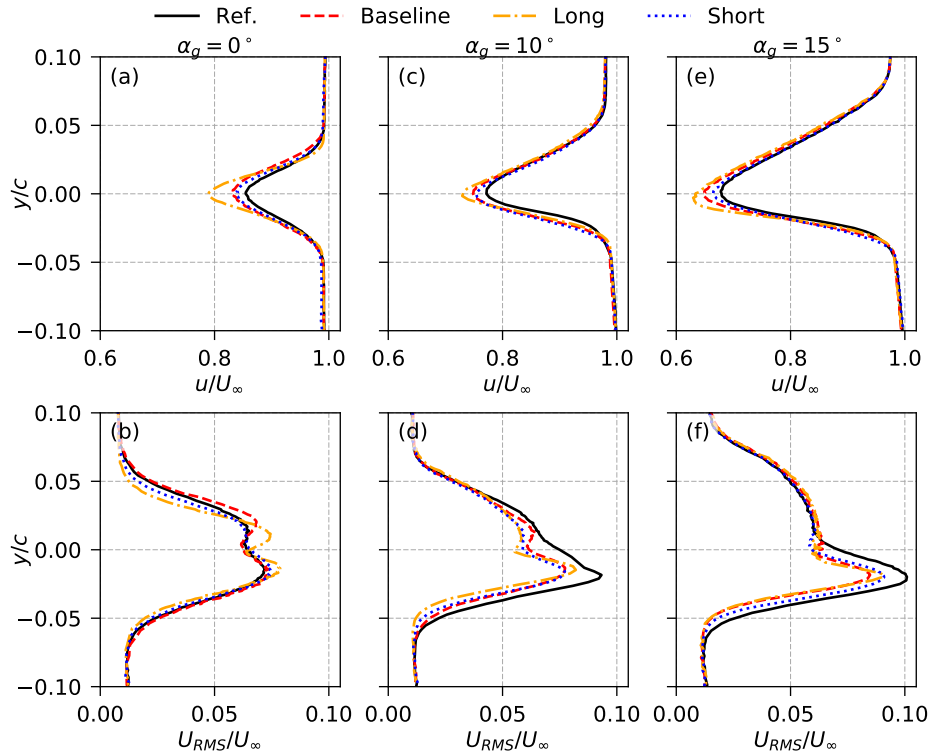

Figure 10: Mean and RMS wake profiles of the streamwise velocity component at $Re_c = 200,000$ for variation in flaplet length.

can be seen at Re_c=250,000 and this is due to the delay in the occurrence of tonal noise, which can be clearly seen in the acoustic spectra (Fig. 6b). At Reynolds numbers beyond 500,000 it is seen that the baseline flaplets do not show too much, if any, OSPL reduction, which is due to the tonal noise in both the reference and baseline cases being approximately the same. As was seen at $\alpha_g = 0°$, the OSPL for the short flaplets tends towards the value for the reference aerofoil as the Reynolds number increases. Increasing α_g further to 15° reveals similar effects as those seen for both lower angles, although the effects are less pronounced. At Reynolds numbers below 400,000 it can be seen that both the short and baseline flaplets show an OSPL reduction of around 2.5 dB, after which the reduction increases. This is again due to the lower tonal noise component observed with the flaplets.

In order to observe the effect of the flaplets on the wake flow, hot wire measurements were taken at a streamwise distance of $0.25c$ aft the solid

trailing edge. Therefore, no offset has been taken into account for the flaplets length. Figures 10a-c-e show mean streamwise velocity profiles for each of the flaplets of varied length at each of the tested angles of attack at $Re_c = 200,000$. At $\alpha_g = 0°$, the profile is symmetric about the $y/c = 0$ line. This is expected as the aerofoil is symmetric itself, the wake deficit should also be symmetric here. As the angle is increased, the wake profiles become thicker on the suction side of the aerofoil ($y/c > 0$), which is due to the thickening of the boundary layer on this side of the aerofoil. In addition, the absolute value of the velocity deficit is also seen to increase at higher angles, from a value of $u/U_\infty = 0.85$ for the reference aerofoil at $\alpha_g = 0°$ to a value of around 0.7 for the same aerofoil at $\alpha_g = 15°$ It can be seen that at each of the angles the largest velocity deficit is visible for the long flaplets followed by the baseline and then the short flaplets. This is a logical conclusion as there was no offset for the flaplet length, hence the tip of the long flaplet was physically closer to the probe. A more discernible difference between flaplets and reference aerofoil can be seen when looking at the streamwise RMS profiles as shown in Figs. 10b-d-f. At $\alpha_g = 0°$ it can be seen that all RMS profiles are similar, even with those obtained for the baseline and the long flaplets showing a small increase compared to the reference aerofoil. As the angle increases to $\alpha_g = 10°$, Fig. 10d, a peak in the RMS velocities can be seen on the pressure side of the aerofoil. This is very evident for the reference aerofoil and is attributed to be due to the high levels of turbulence caused by the separation and reattachment of the separation bubble on the pressure side of the aerofoil close to the trailing edge. All of the flaplet cases show some reduction in the RMS velocities and are of similar amplitude. Increasing the angle further, again shows a similar level of reduction for each of the tested cases. Therefore it is clearly seen that the flaplets indeed modify the turbulent fluctuations in the wake at $\alpha_g = 10°$ and $15°$. Interestingly, there also does not seem to be a length dependency in this reduction.

In order to obtain a better understanding about how the flaplets are modifying the wake structures, spectra of the turbulent velocity fluctuations, taken at the point of maximum RMS observed in Fig. 10f, will be analysed. This point was specifically chosen as it corresponds to the approximate position of the centre of the shed vortices. Also, an angle of $\alpha_g = 15°$ was selected for this analysis, as the velocity spectra at the lower angles showed influences from the tonal noise observed in the acoustic spectra, and as such the trends were not as clear as those shown in Fig. 11. The spectra correspond to the vertical fluctuating velocity component, v', as this can be assumed

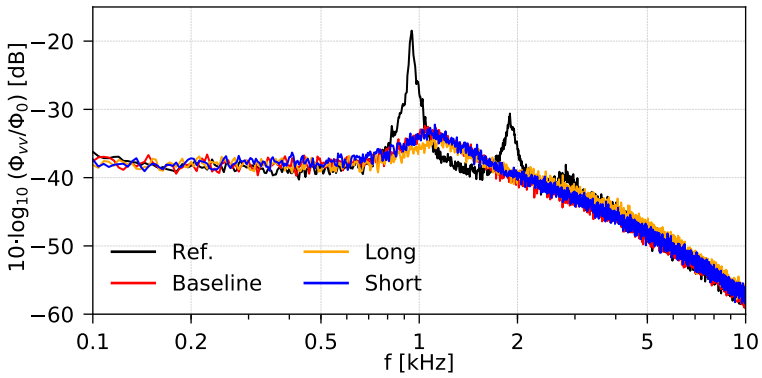

Figure 11: Fluctuating vertical velocity component, v', turbulence spectra (ϕ_{vv}) normalised with a nominal $\phi_0 = 1$ m^2/s at the peak RMS point in wake profiles at $\alpha_g = 15°$ and $Re_c = 200,000$ for variation in flaplet length.

to be more sensitive to spanwise structures, such as shed vortices from an aerofoil. In addition, it is known that this so-called "upwash" velocity is a significant parameter that determines the generation of noise at the trailing edge [32]. When looking at the results for the reference aerofoil, it can be clearly seen that there is a strong dominant peak at 950 Hz, and the subsequent secondary and tertiary harmonics at 1850 Hz and 2850 Hz respectively. Observing the resulting velocity spectra obtained for the three flaplet cases immediately reveals that there is a clear, almost complete reduction in this peak. The remaining hump has been shifted to a slightly higher frequency, $\approx$ 1100 Hz, and it is more broadband in nature. Where this broadband hump is more or less identical for the baseline and short flaplets, with the shedding being slightly reduced for the longest flaplets.

In a subsequent experiment the motion of the flaplets was non-intrusively measured using a laser displacement sensor. Using this technique enlightens the motion of a single flaplet at the different tested Reynolds numbers; herein the results just at $\alpha_g = 0°$ are presented. Figure 12, shows the spectra of the motion of the flaplets as they oscillate in the flow. It should be noted here that a small vibration from the model could be detected and the frequency of this oscillation has been indicated on Fig. 12 as a vertical grey bar at $f \approx 80\ Hz$. The RMS of the model vibration (y_{rms}), measured at $x = 0.9$c and at $Re_c = 900,000$, was $y_{rms} = 0.015$ mm, and a maximum peak to peak vibration of $y = 0.1428$ mm. In comparison the corresponding y_{rms} of the baseline flaplets at the same condition was $y_{rms} = 0.060$ mm, and

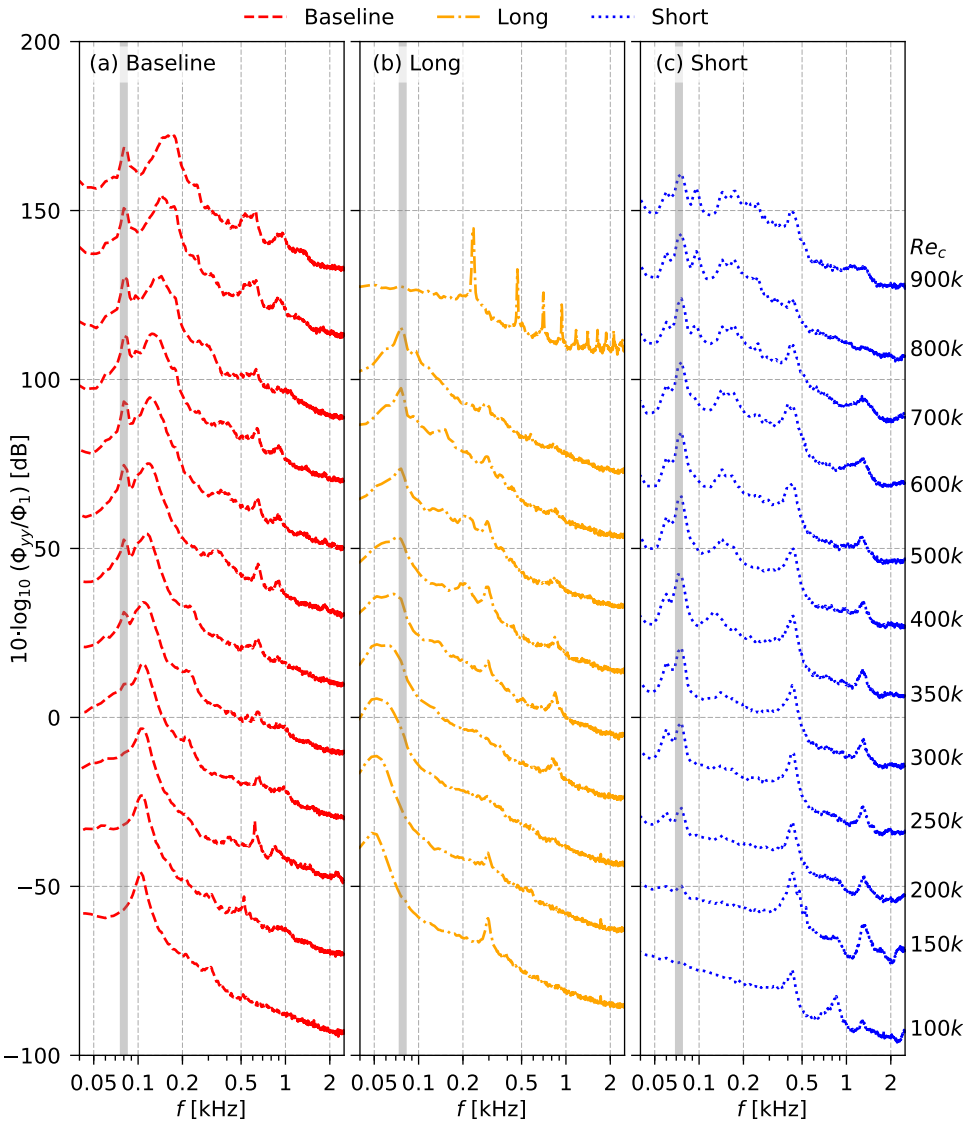

Figure 12: Spectra of the laser displacement measurements, (ϕ_{yy}) normalised with a nominal $\phi_1 = 1$ m^{2}s at $\alpha_g = 0°$ for variation in flaplet length.

a maximum peak to peak of $y = 0.611$ mm. Fig. 12a, shows the results for the baseline flaplets, and it can be immediately clear that at the lowest Reynolds number there is a clear peak just above $f = 110$ Hz, and this corresponds to the Eigen frequency of the flaplets, as can be seen in Table 2.

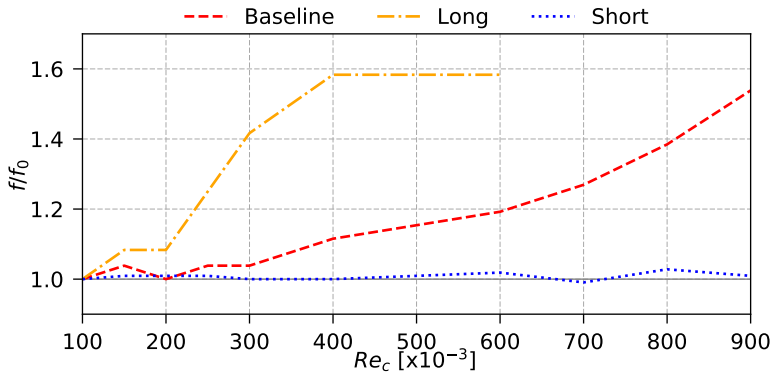

Figure 13: Normalised flapping frequency, with the respective Eigen frequency f_0, as Reynolds number increases at $\alpha_g = 0°$ for variation in flaplet length.

As the Reynolds number increases the flaplet oscillation persists, however it can be seen that the frequency of oscillation becomes more broadband and increases in frequency. It is also interesting to observe a smaller secondary peak at $f \approx 700$ Hz, which when referring back to Table 2, can be seen as the secondary bending mode frequency. At the highest two Reynolds numbers this peak becomes broader, which could indicated that the flaplets are close to their critical velocity, or close to flutter.

When looking at the long flaplets, Fig. 12b, the Eigen frequency peak can be clearly seen at $f \approx 50$ Hz. In a similar way as the baseline flaplets, the frequency of the oscillation increases with Reynolds number. Here it should be noted that the exact frequency of the oscillation at the higher Reynolds numbers cannot be clearly distinguished from the model vibration. Looking at the second peak, it is again coincident with the second bending mode frequency ($f = 284$ Hz) and it can be seen to persist with increasing Reynolds number. As was seen in the acoustic spectra, the long flaplets once again go into flutter at high Reynolds numbers. The frequency of the flutter here is measured to be $f = 230$ Hz, which is in reasonable agreement with the predicted flutter frequency ($f_f = 187$ Hz).

Finally in Fig. 12c, the short flaplets are also observed to oscillate at their Eigen frequency across all Reynolds numbers.

An interesting difference here is that the frequency of oscillation stay more or less constant throughout the entire Reynolds number range, which is in stark contrast to the other two length, which both increase their oscillation frequency with Reynolds number, as can be seen in Fig. 13. This could

indicate that here the Eigen frequency is too high to lock-in with structures in the flow, whereas the other lengths are able to lock-in with some low frequency structures in the flow.

3.3.2. Variation in Flaplet Width

The next parameter varied was the spanwise width of the flaplets. At $\alpha_g = 0°$, Fig. 14, it can be seen that for the cases up to Re_c=500,000 the low frequency reduction is most prominent when the wide flaplets are attached. This is followed by the baseline flaplet and then the narrow flaplets. For higher Reynolds numbers, the wide flaplets sound pressure level gradually increase above that of the reference case in the low frequency region, and then at Re_c = 700,000 the flaplets begin to flutter in a similar manner to the long flaplets. The frequency of the flutter heard in the acoustic spectrum here was in the f_c = 250 Hz band, which is in reasonable agreement with predicted flutter velocity in Table 2, f_f = 343 Hz. When observing the high frequencies, the reverse of the low frequency effect is observed, where the wide flaplets show the largest noise increase, followed by the baseline and the narrow flaplets. This is assumed to be due to the narrow flaplets being able to more successfully disrupt the small scale structures (due to their geometrical size) and vice versa for the low frequency reduction and the wide flaplets.

At $\alpha_g = 10°$, the low frequency reduction of the wide flaplets is comparable to that of the baseline flaplets, whereas the high frequency increase for the wide flaplets is still higher than that of the baseline flaplets. When tonal noise occurs, it can be seen that all the cases cause a delay and once again show a reduction. It is important to note that the narrow flaplets do not show any tonal noise across the whole Re_c range. This is indicating that the narrow elements severely disrupt the acoustic feedback loop and the instabilities within the boundary layer on the pressure side of the aerofoil. Increasing the angle to $\alpha_g = 15°$ yields similar trends to those at lower angles. The exception is that the wide flaplets reach a higher Reynolds number before they go into flutter.

When looking at the ΔL_p contours in Figure 15, it can be seen that the regions of low frequency reduction are the same for all of the width cases at all angles of attack. The difference is that the magnitude of the reduction is clearly highest with the wide flaplets and lowest with the narrow flaplets. This is showing that the width plays a strong roll in the noise reduction at these low frequencies, where as the length shifts the reduction zones as

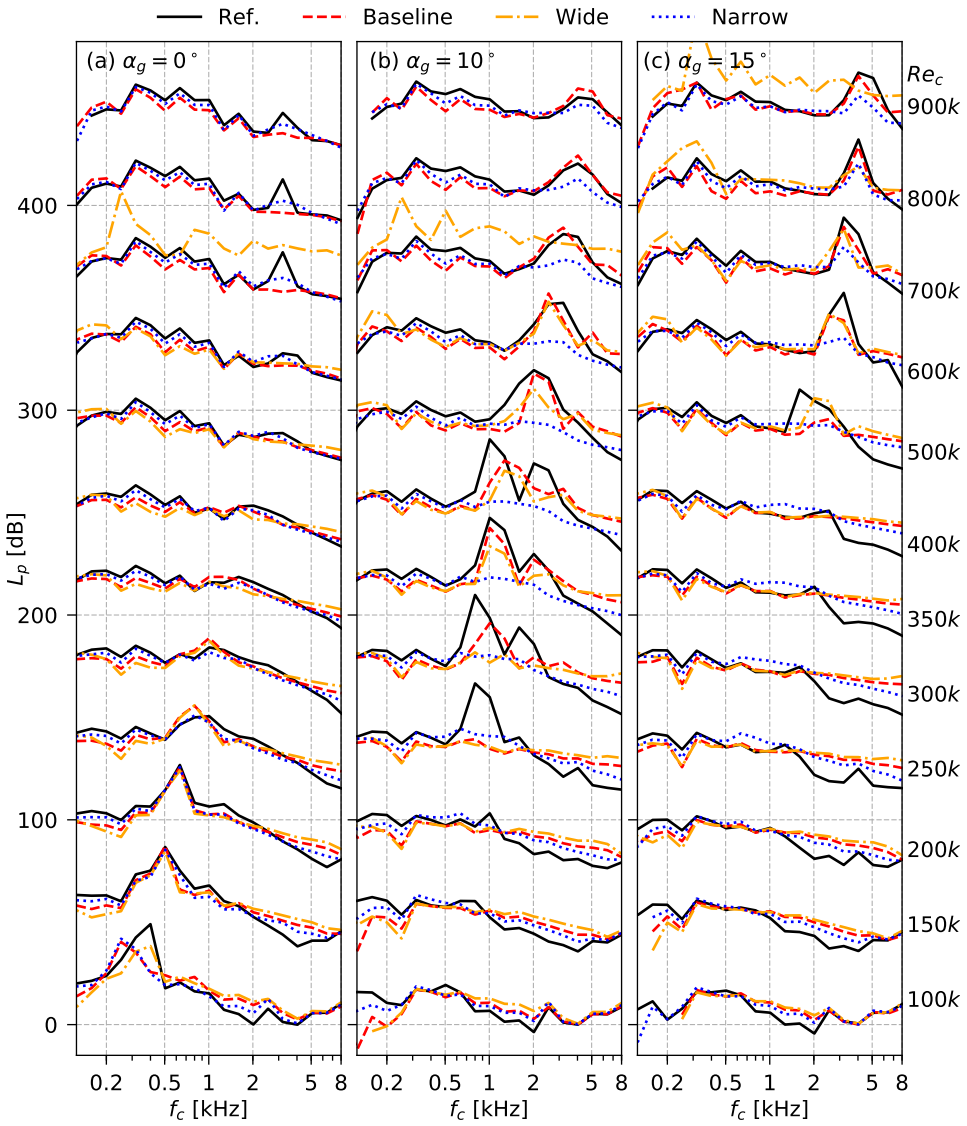

Figure 14: 1/3 Octave band acoustic spectra for variation in flaplet width. Each of the spectra are spaced with 35 dB from each other for clarity.

was seen in Fig. 7. This trend of increased magnitude of reduction when the width was also observed by the analytical model of Gruber et al. [18] for slitted serrations, hinting that indeed the geometry of the flaplets does indeed play a key role in this low frequency reduction.

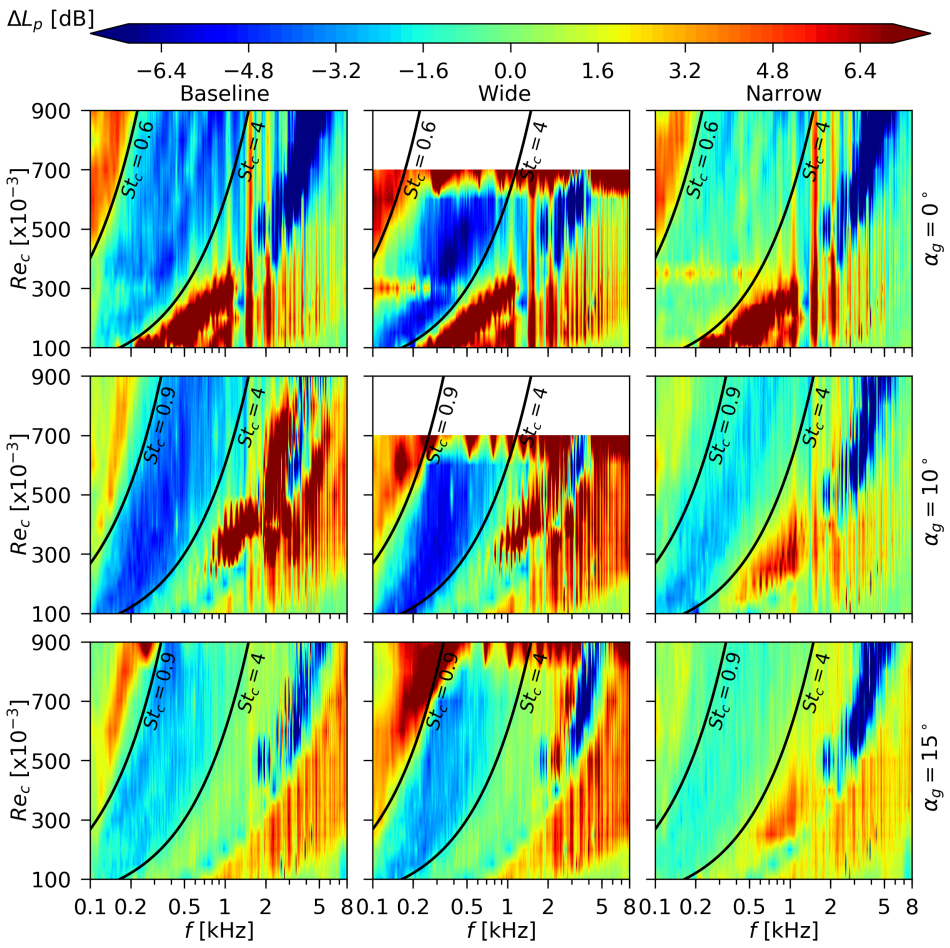

Figure 15: ΔL_p contours for variation in flaplet width, with the zone of maximum reduction indicated.

When looking at the sound maps for this geometric variation, Fig. 16, at f_c=1 kHz the clear tonal noise reduction that was seen in Fig. 14b is seen with both the wide (c) and narrow (d) flaplets. The narrow flaplets show a significant reduction of up to 40 dB. At f_c=8 khz, it can be clearly seen that the width of the flaplets has a strong effect on the high frequency acoustic scattering. The wide flaplets (g) show a strong acoustic source across their surface, the strength of which decreases with reducing flaplet width, yielding a significantly lower acoustic source for the narrow flaplets (h) which is almost 15 dB lower than for the wide flaplets. This again is showing that this high

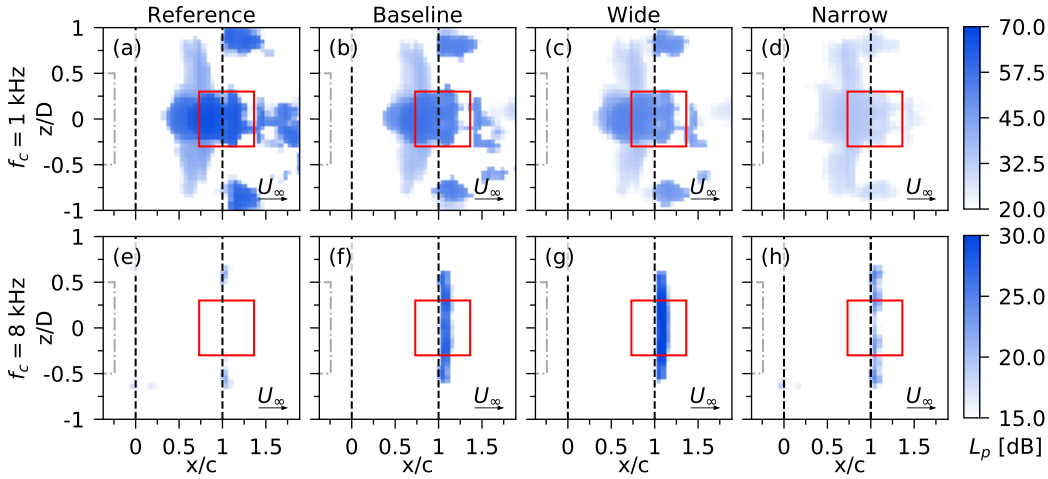

Figure 16: 2D sound maps as the flaplet width is varied, at Re_c=350,000 and $\alpha_g = 10°$. (a–d) shows the frequency band, f_c=1 kHz and (e–h) shows the frequency band, f_c = 8 kHz. (- · - · -) indicates the jet nozzle, (- - -) indicates the aerofoil, (——) indicates the interrogation region for acoustic spectra.

frequency noise is a function of the flaplet surface area.

When looking at the ΔOSPL at $\alpha_g = 0°$, Fig. 17b, the narrow flaplets show a constant reduction of 2 dB across most of the tested velocity range. The wide flaplets show a similar trend as the baseline flaplets, but at each Reynolds number below 400,000 there is more of a reduction. This corresponds to the greater low frequency reduction observed in Fig. 14a. Of course this trend ceases as the wide flaplets start to flutter. At $\alpha_g = 10°$, it can be seen that for the low Reynolds number cases, up to $Re_c = 250{,}000$, the narrow flaplets are not as efficient as the baseline and wide flaplets. However after this point, when tonal noise is present, the narrow flaplets significantly outperform all other flaplet cases, with maximum reductions in the order of 20 dB observed. As the tonal noise disappears for the reference aerofoil, the noise reduction tends towards 2.5 dB. Reductions of the OSPL can also be seen for the baseline and wide flaplets due to the slight suppression of the tonal noise component and low frequency reductions. As the angle increases further to $\alpha_g = 15°$, reductions can be seen for all flaplets, and again the maximum reductions are visible when tonal noise is present on the reference aerofoil.

When looking at the hot wire measurements, the mean profiles in Figs. 18a-c-e show that the flaplets all lead to a similar wake deficit. Comparing the

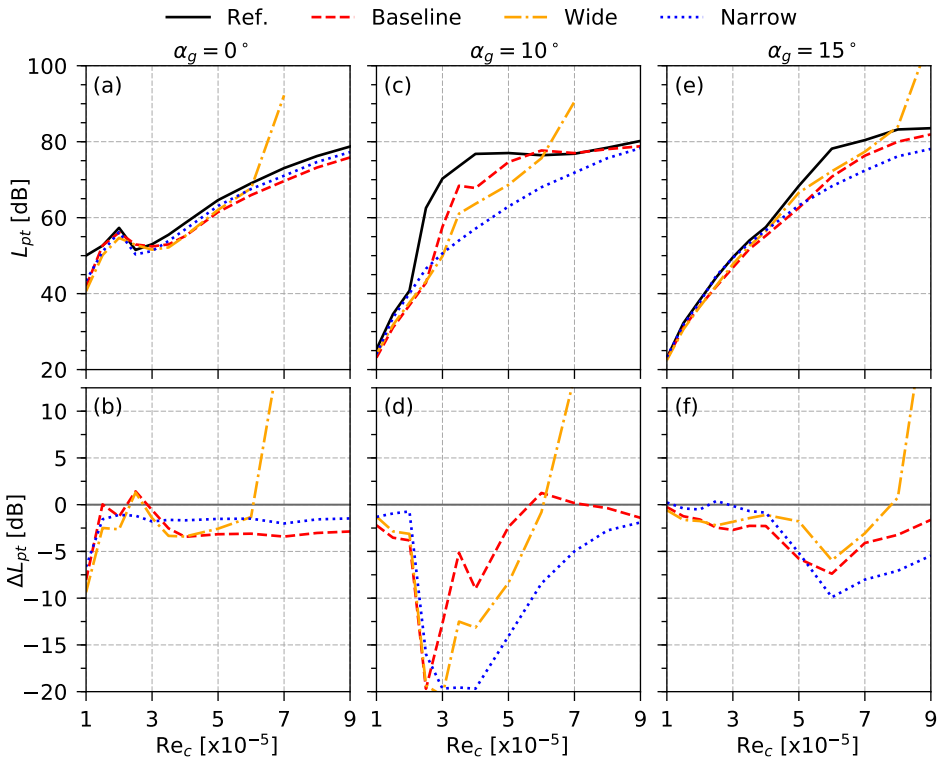

Figure 17: OSPL, denoted as L_{pt}, and Delta OSPL, ΔL_{pt}, for variation flaplet in width.

results with the wake deficit differences observed in Section 3.3.1 for the flaplets of varying length leads to the conclusion that the differences there are only due to the geometrical variation of the length and not of the width. When looking at the RMS velocity profiles in Figs. 18b-d-f, an interesting result can be seen in Fig. 18f, where there is a clear order of the magnitude of the RMS velocity on the pressure side of the aerofoil. It can be seen that the narrow flaplets dampen the turbulence in the wake most effectively, whilst the wide flaplets dampen the least. Nevertheless, there is still a moderate reduction in comparison to the reference aerofoil.

Figure 19 then shows turbulence spectra measured in the wake. A clear peak is visible at ≈ 0.95 kHz for the aerofoil with narrow flaplets. As the width of the flaplets is increased to the baseline width, it can be seen that the width of this peak increases as well, while the peak amplitude decreases. This trend continues, until the peak is almost completely removed for the aerofoil with wide flaplets. In order to get a more detailed understanding of

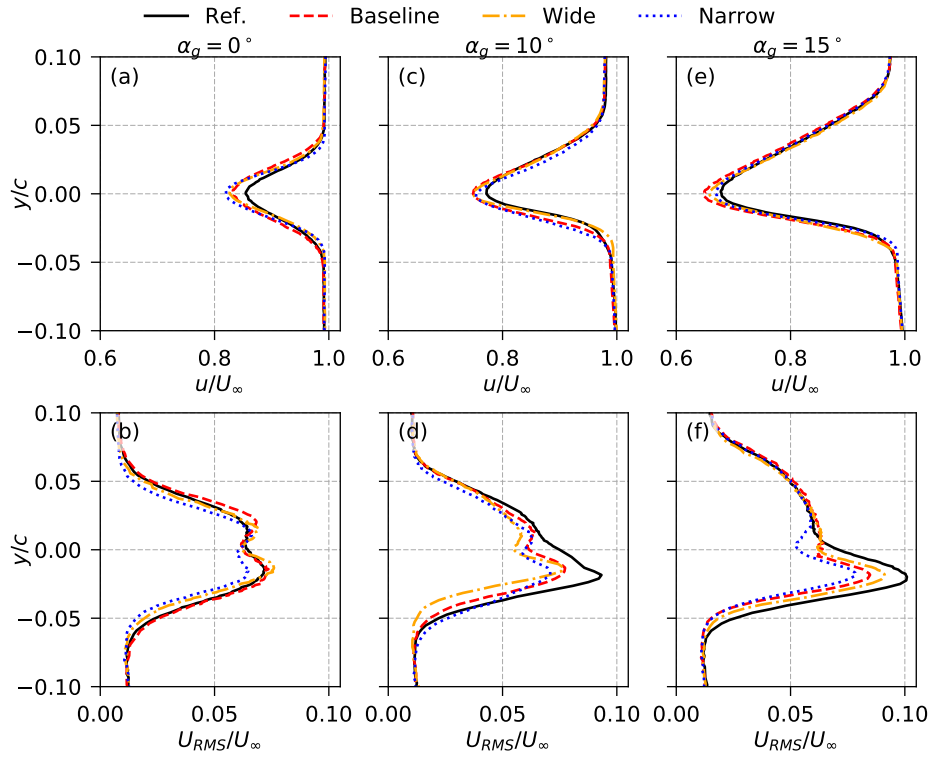

Figure 18: Mean and RMS wake profiles of the streamwise velocity component at $Re_c = 200,000$ for variation in flaplet width.

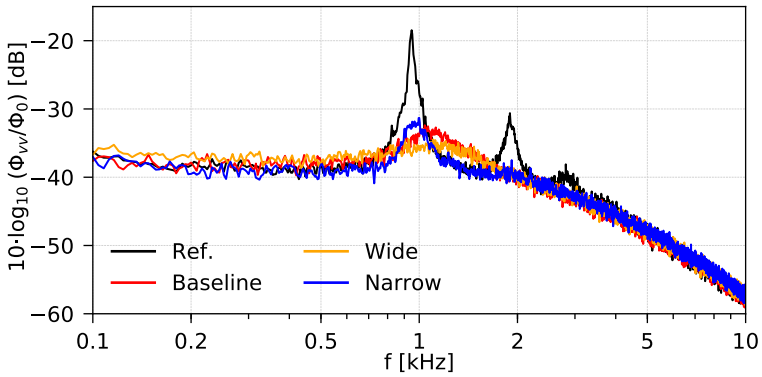

Figure 19: Fluctuating vertical velocity component, v', turbulence spectra (ϕ_{vv}) normalised with a nominal $\phi_0 = 1$ m^2/s at the peak RMS point in wake profiles at $\alpha_g = 15°$ and $Re_c = 200,000$ for variation in width.

the wake modification, the energy per mass unit associated with the vortex shedding, E_{vs}, will be compared for the different cases. This is simply done by calculating the integral of the velocity spectra for the frequency band that contains the peak according to:

$$E_{vs} = \int_{f_{vs,L}}^{f_{vs,U}} \Phi_{vv}(f)\ df, \tag{4}$$

where $f_{vs,U}$ and $f_{vs,L}$ are taken to be $\pm$ 200 Hz from the peak in the spectra and Φ_{vv} is the result of the fast Fourier transform (FFT).

It must be noted here that it is only feasible to compare the different flaplet cases with each other, but not with the reference aerofoil without flaplets. This is due to the fact that the distance between the hot wire measurement location and the point where the vortices are shed is different, as the distance from the solid trailing was kept constant and no additional offset was made for the flaplet length (by the same logic, the integral was not computed for the varying length case to avoid any incorrect conclusions).

The resulting energy associated with the vortex shedding is 0.158 m^2s^{-2} for the baseline flaplets, 0.107 m^2s^{-2} for the wide flaplets and 0.139 m^2s^{-2} for the narrow flaplets. As was expected, the energy is the lowest for the wide flaplets. However, the energy for the reference flaplets is higher than that of the narrow flaplets. This is due to the fact that the magnitude of the observed peak is approximately the same as that for the baseline flaplets, while the peak width is much greater for the baseline case. Thus, the energy is seen to be higher with the integration limits used. In total, all the flaplets effectively reduce the vortex shedding, and as the width of the peak is increased, the vortices seem to decay faster. A similar observation was made by Yu and Yang [33] in their simulation.

When looking at the flaplets oscillation spectra, Figure 20, it can be seen that all the flaplets have a main peak at their Eigen frequency, which all are at $f \approx 110$ Hz for this geometric variation due to them all having the same length as each other. The main difference with these flaplets is the 1st torsional mode frequency, as seen in Table 2, where the wide flaplets have a much lower torsional frequency, $f_{1^{st}T} = 494$ Hz, in comparison to the baseline and narrow flaplets. This torsional frequency can be seen in to emerge in Fig. 20b, from $Re_c = 350,000$ onwards. This frequency can be seen to increase as the Reynolds number is increased. In the acoustic spectra it was observed that the wide flaplets went into flutter at $Re_c = 700,000$, and the results in

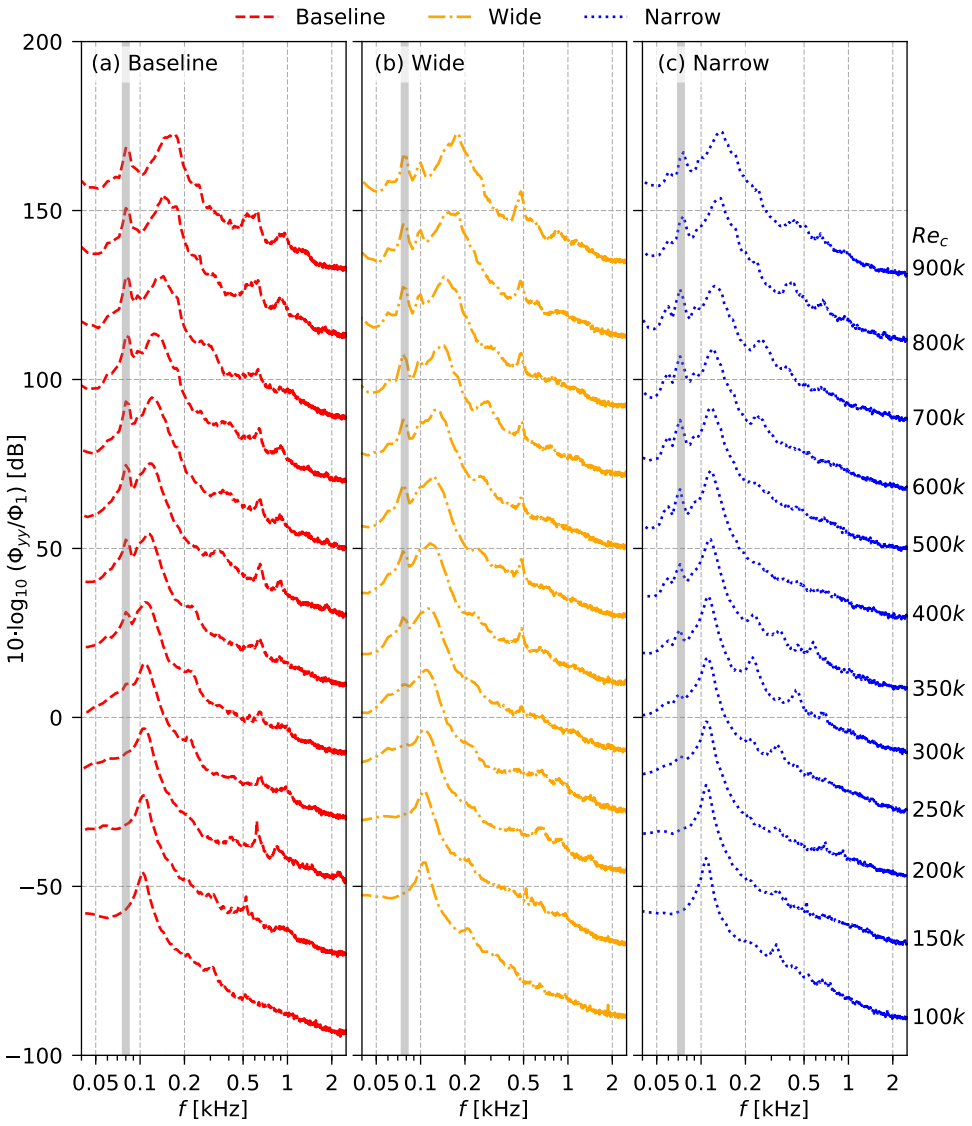

Figure 20: Spectra of the laser displacement measurements, (ϕ_{yy}) normalised with a nominal $\phi_1 = 1$ m^{2}s at $\alpha_g = 0°$ for variation in flaplet width.

Fig. 20 show that the flutter here is due to the coupling of the torsional and bending modes. It must be noted here that the flutter was not observed in this experiment showing that this process of jumping to flutter is sensitive, and a possible reason for this could be due to a different mounting mechanism

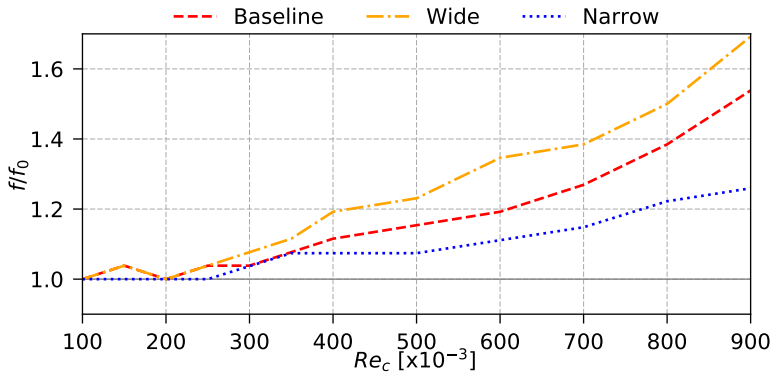

Figure 21: Normalised flapping frequency, with the respective Eigen frequency f_0, as Reynolds number increases at $\alpha_g = 0°$ for variation in flaplet width.

of the aerofoil for this experiment.

Another observation can be seen in Fig. 21 between the different flaplets is that the Eigen frequency of the narrow flaplets does not increase as much as the baseline and the wide flaplets as the Reynolds number increases. This finding alludes to the fact that the wide and baseline flaplets are better at locking in to the large scale structures in the wake and reducing the vortex shedding, as was observed in Fig. 19.

3.3.3. Variation in Flaplet Inter-Spacing

The variation of the inter-spacing of the flaplets is in effect a way to alter the 'porosity' of the flaplets. The changes in the spacing are detailed in Table 1, and it can be seen that the smallest spacing is that of the baseline flaplets (1 mm) followed by the medium spacing (3 mm) and large spacing (7 mm). The large spacing flaplets are spaced such that every other flaplet, from the baseline case, is removed. At $\alpha_g = 0°$, Fig. 22a, the flaplets generally behave in a similar manner to each other. However, it is clear that the smallest spacing (baseline) has the most reduction in the low frequency range, whereas the medium and the large spaced flaplets show only a small or no reduction in this range. As is seen with all other tested cases, the flaplets do lead to an increase of noise in the high frequency range, the largest spacing inducing the smallest increase. When looking at the trailing-edge bluntness noise ($Re_c > 600{,}000$ at $f_c = 3$ kHz), the baseline and medium flaplets show a reduction whereas the flaplets with large spacing show only a small reduction with regards to the baseline. These results are explained by the

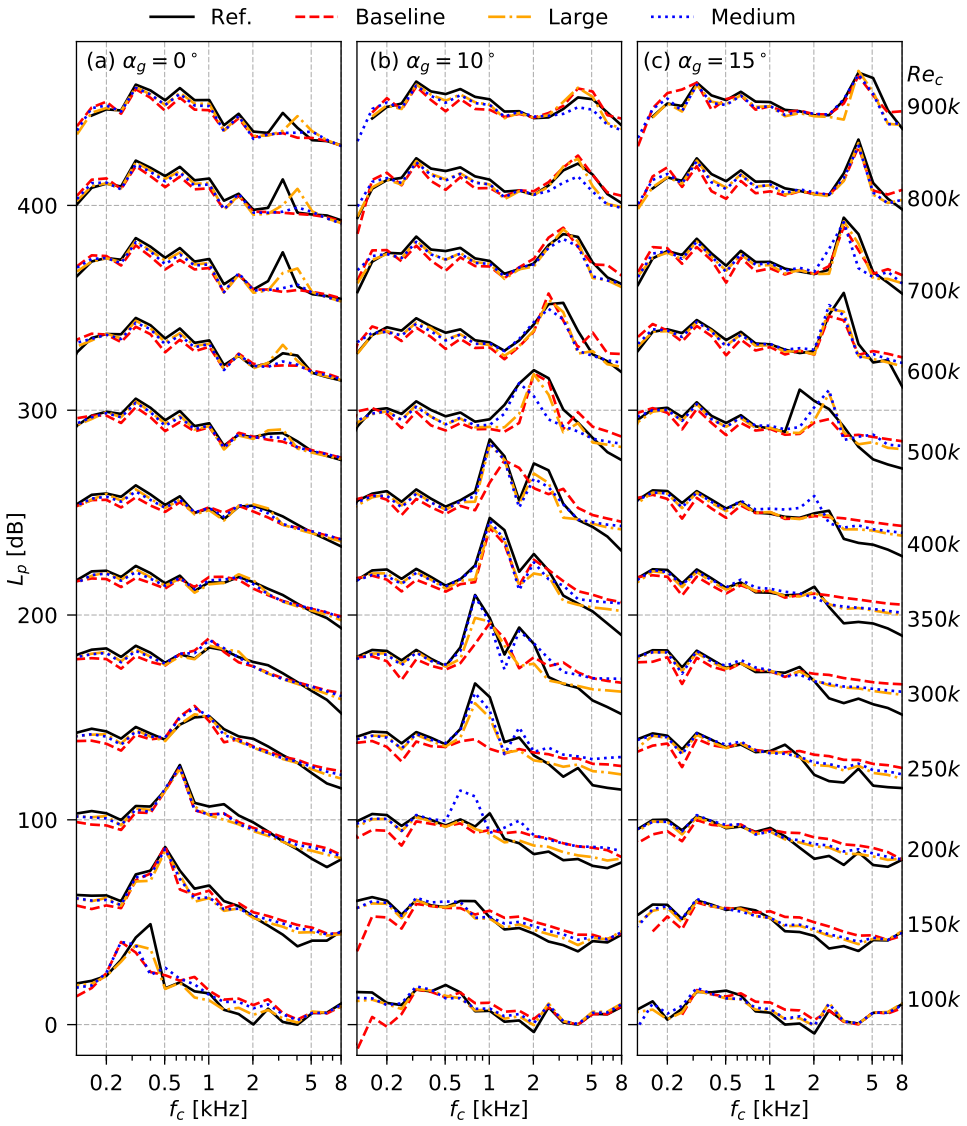

Figure 22: 1/3 Octave band acoustic spectra for variation in flaplet inter-spacing. Each of the spectra are spaced with 35 dB from each other for clarity.

fact that there is more trailing edge exposed, therefore the acoustic effect of the bluntness is more pronounced.

Increasing the angle to $\alpha_g = 10^\circ$ and 15° shows similar effects, and as in the previous geometric variations, the magnitude of the effects are enhanced.

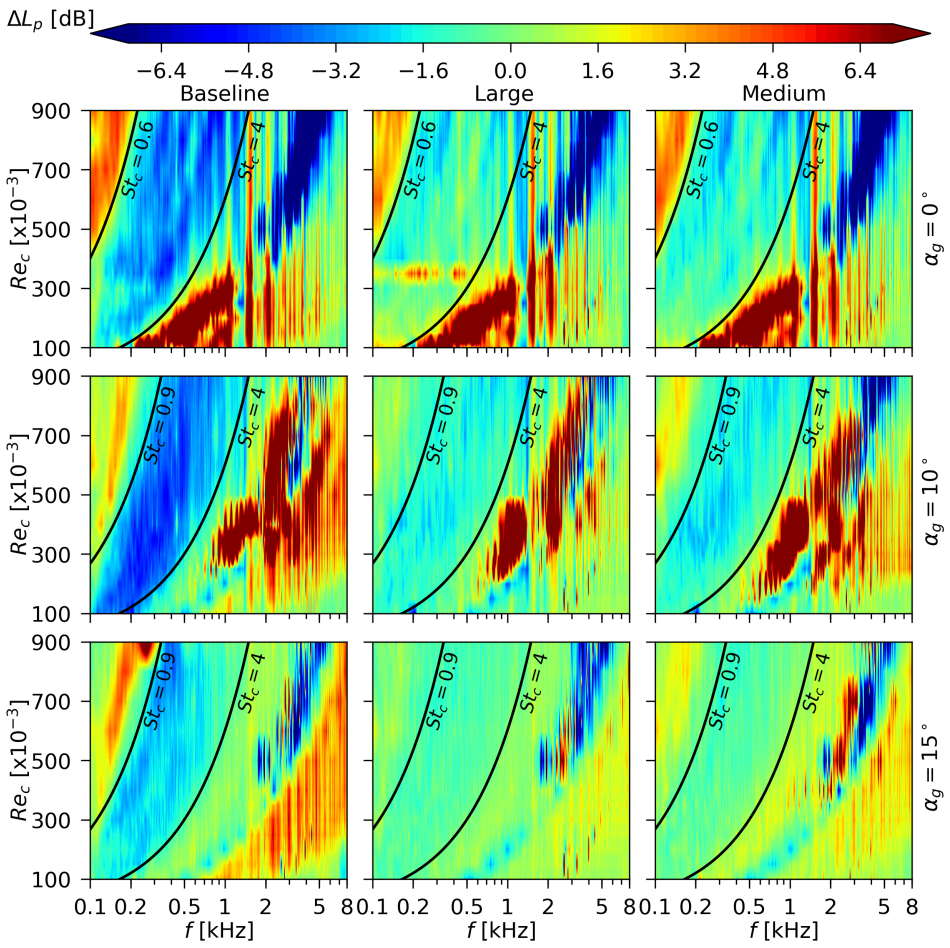

Figure 23: ΔL_p contours for variation in flaplet inter-spacing, with the zone of maximum reduction indicated.

The ΔL_p contours in Figure 23, again show that the reduction zone is dependent on the length only. The magnitude of the reduction zone shows that there is quite a large drop off in effectiveness when the inter-spacing is increased to the medium inter-spacing and again even further when the large spacing is used. The large drop off in effectiveness was also seen by Gruber et al. [18] once the spacing between the slitted serrations was increased.

The sound maps for the 1 kHz band shows very little difference between the different spacings. At 8 kHz, it can be seen that as the spacing increases from the smallest (baseline case (f)) to the largest (g) the acoustic source

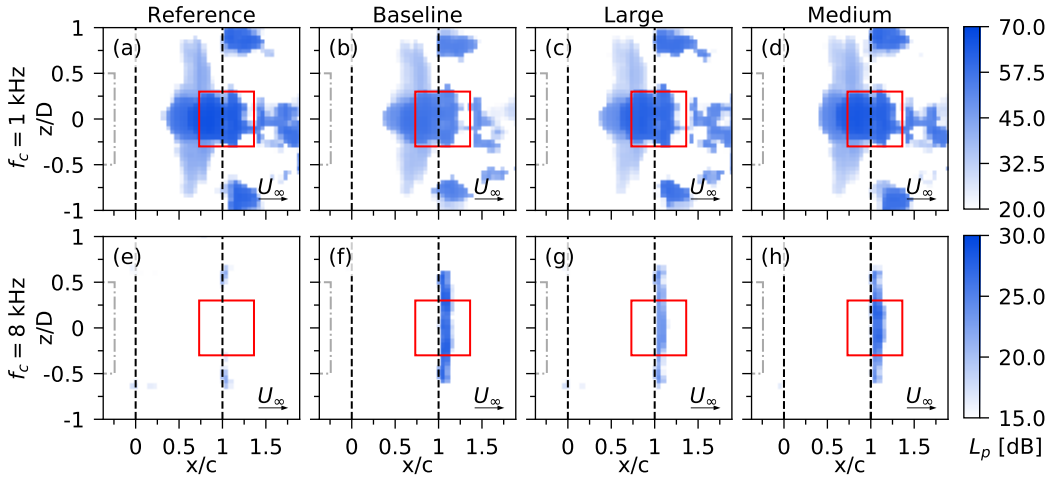

Figure 24: 2D sound maps as the flaplet inter-spacing is varied, at Re_c=350,000 and $\alpha_g = 10°$. (a–d) shows the frequency band, f_c=1 kHz and (e–h) shows the frequency band, f_c = 8 kHz. (- · - · -) indicates the jet nozzle, (- - -) indicates the aerofoil, (——) indicates the interrogation region for acoustic spectra.

located at the flaplets decreases in strength, again as with the other geometric variations this is due to the reduced flaplets surface area.

When looking at the OSPL and the ΔOSPL at $\alpha_g = 0°$, Fig. 25a-b, it is visible that at flow velocities for which tonal noise ceases to occur ($Re_c > 300,000$) there is a clear reduction of noise for all flaplets. Thereby, the magnitude of the reduction increases as the spacing is reduced. A 'steady' reduction of ≈ 3.5, 2.5 and 2 dB for each of the cases can be seen, in the order of inter-spacing distance. This shows that, although the smallest spacing increases the high frequency noise the most, the low frequency noise reduction is sufficiently large enough to compensate and yield this moderate overall reduction. At $\alpha_g = 10°$, the tonal noise reduction is the dominant contribution to the overall noise reduction. Increasing the angle further shows an interesting result, where the medium spaced flaplets show no overall reduction until $Re_c = 500,000$ where the reduction is again due to the suppression of the tonal noise component. For this geometric constraint it can clearly be seen that, generally, the smallest spacing is the most efficient across all the tested cases.

Figure 26 shows the hot wire measurement results for this geometric variation. Again, as seen with the width variation, the difference observed is due to the elongation of the effective trailing edge. Looking at the RMS velocity

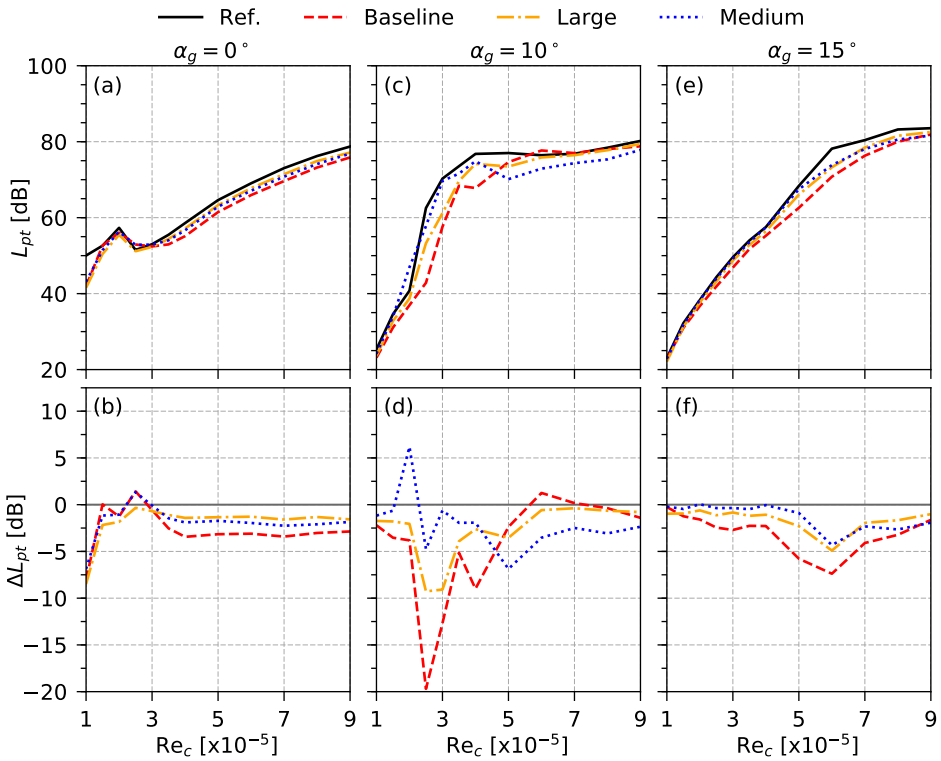

Figure 25: OSPL, denoted as L_{pt}, and Delta OSPL, ΔL_{pt}, for variation in flaplet inter-spacing.

profiles, again little difference is seen between inter-spacing at $\alpha_g = 0°$ and 10°. However, further increasing the angle to 15° again shows a clear difference between the spacings, where the smallest spacing (baseline flaplets) leads to the smallest RMS values. As the spacing increases, the RMS velocity profile tends back towards that of the reference case, which is to be expected.

When looking at the turbulence spectra in the wake, shown in Fig. 27, it is immediately obvious that as the inter-spacing is increased, the spectral shape tends back towards that of the reference case without flaplets, as the vortex shedding peak increases. This is reflected in the resulting shedding energy calculation according to Eqn. 4, where the baseline flaplets yield a value of 0.158 m^2s^{-2}, the medium spacing 0.294 m^2s^{-2} and the large spacing 0.365 m^2s^{-2}. Therefore it can be further seen that the most 'optimal' configuration of spacing is indeed the shortest spacing.

In the laser displacement spectra, again the Eigen frequency of the flaplets

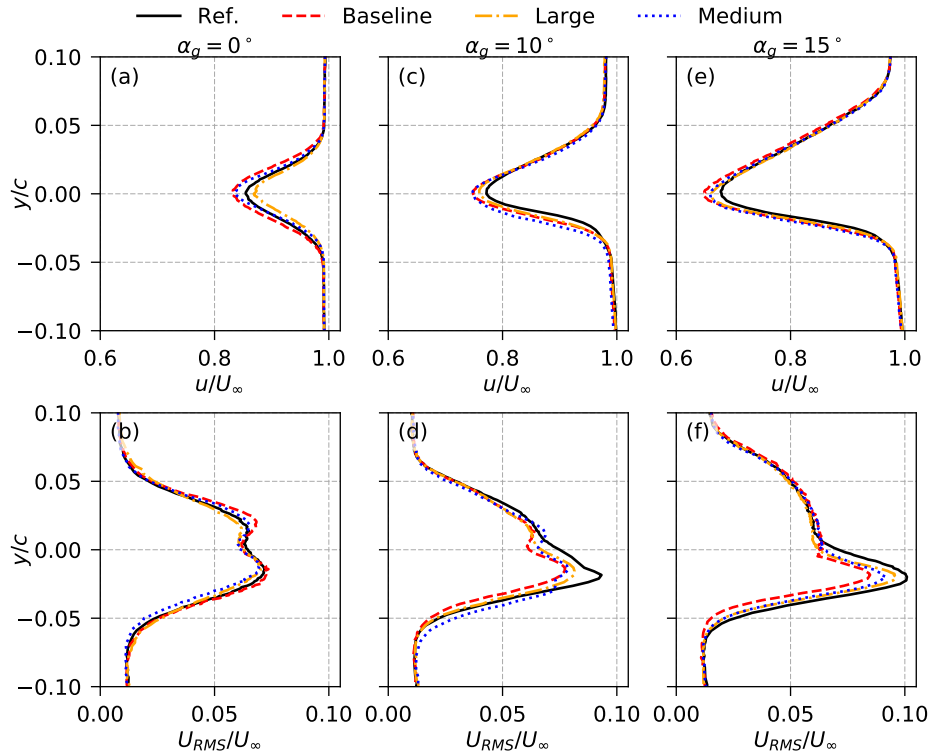

Figure 26: Mean and RMS wake profiles of the streamwise velocity component at $Re_c = 200,000$ for variation in flaplet inter-spacing.

can be easily determined for each of the cases. An interesting results can be observed in Fig. 28b, where at $Re_c = 800,000$, a secondary peak at 280 Hz can be observed, and this does not corroborate with the first torsional or second bending mode, and is unclear what this frequency represents. As the Reynolds number increases further to $Re_c = 900,000$ it was observed that the flaplets started to go into flutter. It should be noted here that the flutter at this testing condition was intermittent, and would periodically go in and out of flutter, therefore seems to be the limiting condition for this arrangement of flaplets. For the medium inter-spaced flaplets, Fig. 28c, at $Re_c = 200,000$ and $250,000$, the tonal noise frequency can be clearly seen to be attenuated in the vibration of the flaplets.

When looking at the frequency shift of the Eigen frequency peaks, Fig. 29, the shift of the flapping frequency of the medium spaced flaplets closely follows that of the baseline flaplets. Until it starts to slightly drift at Reynolds

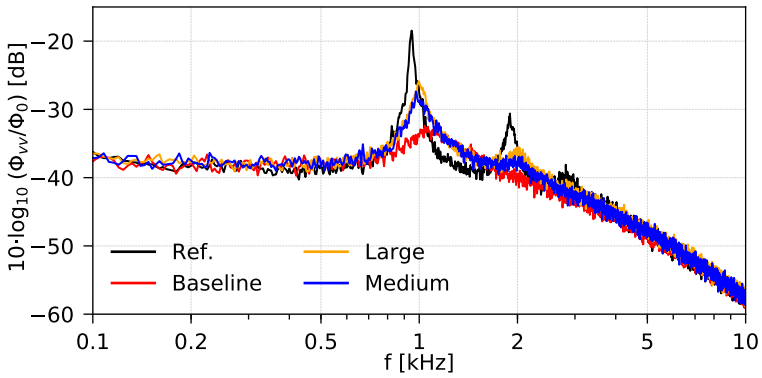

Figure 27: Fluctuating vertical velocity component, v', turbulence spectra (ϕ_{vv}) normalised with a nominal $\phi_0 = 1$ m^2/s, measured at the peak RMS point in wake profiles at $\alpha_g = 15°$ and $Re_c = 200,000$ for variation in flaplet inter-spacing. Each spectrum is spaced by 10 dB for each other for clarity.

numbers above 700,000. Whereas the large spaced flaplets oscillate at the Eigen frequency throughout the test range until $Re_c = 800,000$, where is has a sudden increase in the frequency, prior to flutter.

4. Conclusion

An extensive acoustic study has been carried out on the geometric optimisation of self-oscillating trailing edge flaplets to reduce aerofoil self-noise in a passive way. The effect of a variation of the free vibrating length, width and inter-spacing of these flaplets has been investigated against the reference case of a plain aerofoil. Basically, it has been shown that all flaplets oscillate and reduce the tonal noise to some extent. This has been attributed to the flaplets working as pacemakers, which keep the fundamental instabilities of the T-S waves in the boundary layer flow in their linear state via a lock-in mechanism [21]. Measurements with a laser displacement sensor showed the 1st flexural bending mode being dominant throughout the entire Reynolds number range. Furthermore, hot-wire measurements of the flow in the wake demonstrated that the acoustic results are correlated to the peak levels of turbulence (RMS values of the velocity fluctuation) in the wake. Low turbulence levels mean less tonal noise and vice versa. In a recent study from Yu and Yang [33] it was shown that an oscillating trailing edge fringe is able to reduce the strength and size of the shed vortices, similar as observed for an active oscillation of the trailing edge reported by Simiriotis et al. [34]. A

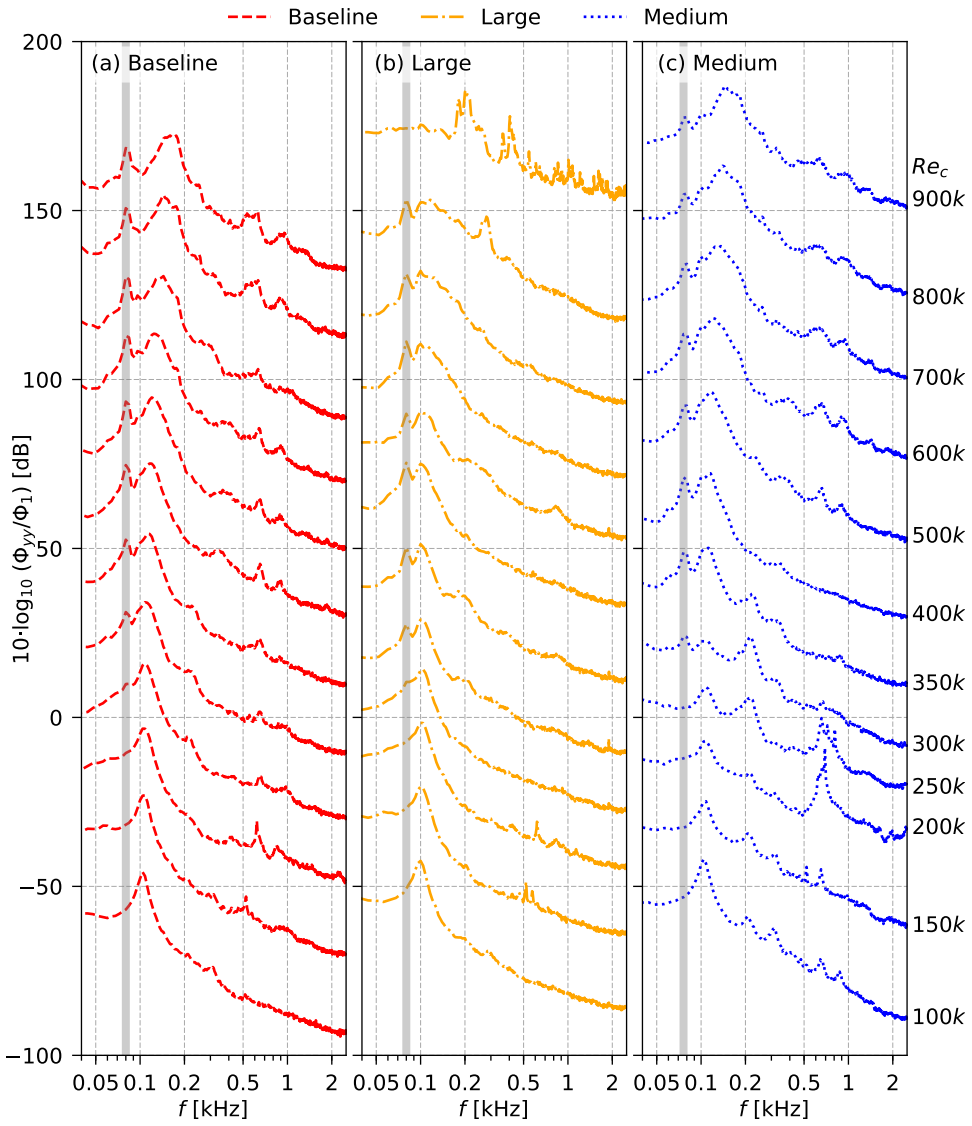

Figure 28: Spectra of the laser displacement measurements, (ϕ_{yy}) normalised with a nominal $\phi_1 = 1$ m^{2}s at $\alpha_g = 0°$ for variation in flaplet inter-spacing.

similar wake-modification can be concluded from the hot-wire measurements for the passive oscillators.

The most effective tonal noise reduction was seen with the narrow flaplets, where almost all tonal components were dampened out. Besides the narrow

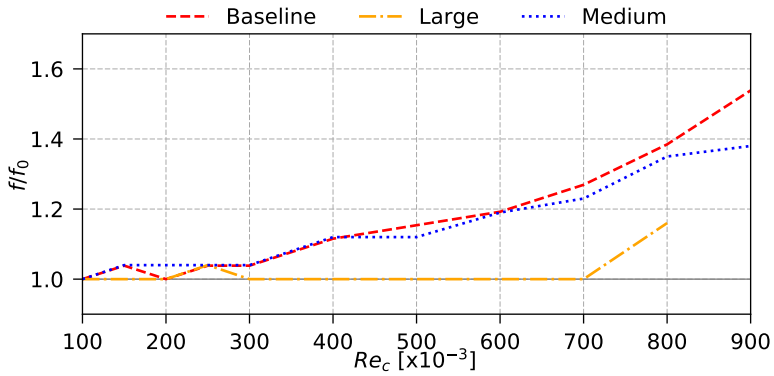

Figure 29: Normalised flapping frequency, with the respective Eigen frequency f_0, as Reynolds number increases at $\alpha_g = 0°$ for variation in flaplet inter-spacing.

flaplets, the short flaplets were also extremely effective at $Re_c > 600,000$. The following list discusses the results for different parameter variations:

- Varying the free vibrating length: This has the most interesting effect, as it changes the natural frequency of the dominant flexural bending mode. When the long flaplets were tested (lower natural frequency), the noise level was reduced at a lower frequency range and vice versa for the short flaplets. Therefore, the range of frequencies where the most reduced noise level is achieved can be tuned by the length of the oscillators.

- Varying the width: Within the low frequency range the widest flaplets had the most effect while the narrow flaplets were least effective, albeit a slight reduction was still observed. It is hypothesized that this is due to the loss of spanwise coherence for the narrow flaplets, which are free to move independently from each other. When increasing the flow velocity (Reynolds number) the widest flaps show an increase in oscillation frequency. This let us conclude that the wider flaplets are locking in with the large scale structures in the wake, affecting the vortex shedding as was further alluded to with the hot wire measurements. In contrast, the motion of the smaller ones is, is rather prescribed by small-scale turbulent structures.

- Varying the inter-spacing: As has been seen already in previous studies by the authors [25, 26], the flaplets with small inter-spacing show

a clear low frequency noise reduction. In this case, the flaplets are effectively 'slit-trailing edge serrations'. A low frequency noise reduction was observed by Gruber et al. [18] with cardboard slit serrations, both experimentally and analytically. While the analytical approach was able to determine multiple frequencies that could be reduced, their experimental results revealed only a single zone where the reduction is observed, similar to the results herein. We would like to point out that it cannot be excluded from their experiments that small vibrations existed, especially as the herein observed acoustic effect is already visible for vibration amplitudes as small as 100-200 μm (compare also the study with active oscillating flaplets with a similar effect at similar oscillation amplitudes, see Simiriotis et al. [34]). Furthermore, their noise reduction was focusing on the broadband noise while the flaplets herein clearly address the tonal noise components.

- Flaps going into flutter: An interesting feature was observed at high Reynolds numbers ($Re_c > 600,000$), where two of the geometries show a sudden massive increase in noise emission. This is attributed to the flaplets going past their critical velocity, at which the torsional bending mode or the second flexural bending mode is excited. Both frequencies could be identified in the spectra prior to the flaplets going into flutter. This causes flow separation and the flaps are no longer effective. Therefore, this constraint must be accounted for in future designs. This could be done either by modifying the flaplets geometry or via the use of non-isotropic materials to prevent the torsional mode.

Following this extensive study, it can be concluded that an optimal flaplet geometry might have a combination of both short and narrow flaplets to see if the benefits of both modifications will hold together and produce an even more effective flaplet configuration. A new practical integrated automated flaplet deployment system is currently in development at City, University of London such that the flaplet length, and hence the Eigen frequency, can be tuned 'on-the-fly' depending on flight conditions. This new automated system is also being investigated with the integration of piezoelectric flaplets where the oscillation can be monitored in real time giving a 'live' view of the flaplets, with potential to view the spanwise interaction of the flaplets. The other benefit of this technology is the application for energy harvesting from the small scale fluctuations of the flaplets in the flow.

Acknowledgements

The position of Professor Christoph Brücker is co-funded by BAE Systems and the Royal Academy of Engineering (Research Chair no. RCSRF1617\4\11) and funding for Mr. E. Talboys to carry out the experiments in Cottbus was made available by The Worshipful Company of Scientific Instrument Makers (WCSIM), both of which are gratefully acknowledged. We also thank Professor Alfredo Pinelli for his hint about a 'pacemaker' mechanism.

References

[1] T. F. Brooks, S. Pope, M. A. Marcolini, Airfoil Self-Noise and Prediction, NASA Ref. Publ. 1218 (1989) 1–142.

[2] R. W. Paterson, P. G. Vogt, M. R. Fink, C. L. Munch, Vortex Noise of Isolated Airfoils, NACA Adv. Restricted Rept. 3G29 J. Aeronaut. Sci. J. Aircr. Low Adv. Ration J. Am. Helicopter Soci-ety J. Aircr. 17 (1972) 3–12.

[3] C. K. W. Tam, Discrete tones of isolated airfoils, J. Acoust. Soc. Am. 55 (1974) 1173–1177.

[4] H. Arbey, J. Bataille, Noise generated by airfoil profiles placed in a uniform laminar flow, J. Fluid Mech. 134 (1983) 33.

[5] M. Lowson, S. Fiddes, E. Nash, Laminar boundary layer aero-acoustic instabilities, in: 32nd Aerosp. Sci. Meet. Exhib., American Institute of Aeronautics and Astronautics, Reston, Virigina, 1994.

[6] A. McAlpine, E. Nash, M. Lowson, On the Generation of Discrete Frequency Tones by the Flow around an Aerofoil, J. Sound Vib. 222 (1999) 753–779.

[7] G. Desquesnes, M. Terracol, P. Sagaut, Numerical investigation of the tone noise mechanism over laminar airfoils, J. Fluid Mech. 591 (2007) 155–182.

[8] S. Pröbsting, F. Scarano, S. C. Morris, Regimes of tonal noise on an airfoil at moderate Reynolds number, J. Fluid Mech. 780 (2015) 407–438.

[9] E. Arcondoulis, C. J. Doolan, A. C. Zander, L. A. Brooks, Y. Liu, An investigation of airfoil dual acoustic feedback mechanisms at low-to-moderate Reynolds number, J. Sound Vib. 460 (2019) 114887.

[10] T. F. Geyer, E. Sarradj, C. Fritzsche, Measurement of the noise generation at the trailing edge of porous airfoils, Exp. Fluids 48 (2010) 291–308.

[11] T. F. Geyer, E. Sarradj, Self Noise Reduction and Aerodynamics of Airfoils With Porous Trailing Edges, Acoustics 1 (2019) 393–409.

[12] M. Herr, Design Criteria for Low-Noise Trailing-Edges, 13th AIAA/CEAS Aeroacoustics Conf. (28th AIAA Aeroacoustics Conf. (2007) 1–14.

[13] A. Finez, E. Jondeau, M. Roger, M. C. Jacob, Broadband noise reduction with trailing edge brushes, Proc. 16th AIAA/CEAS aeroacoustics Conf. (2010) 1–13.

[14] T. P. Chong, P. Joseph, M. Gruber, An Experimental Study of Airfoil Instability Noise with Trailing Edge Serrations, in: 16th AIAA/CEAS Aeroacoustics Conf., volume 332, American Institute of Aeronautics and Astronautics, Reston, Virigina, 2010, pp. 6335–6358.

[15] T. P. Chong, P. Joseph, An experimental study of airfoil instability tonal noise with trailing edge serrations, J. Sound Vib. 332 (2013) 6335–6358.

[16] C. Arce León, R. Merino-Martínez, D. Ragni, F. Avallone, F. Scarano, S. Pröbsting, M. Snellen, D. G. Simons, J. Madsen, Effect of trailing edge serration-flow misalignment on airfoil noise emissions, J. Sound Vib. 405 (2017) 19–33.

[17] C. Arce León, R. Merino-Martínez, S. Pröbsting, D. Ragni, F. Avallone, Acoustic Emissions of Semi-Permeable Trailing Edge Serrations, Acoust. Aust. 46 (2018) 111–117.

[18] M. Gruber, M. Azarpeyvand, P. Joseph, Airfoil trailing edge noise reduction by the introduction of sawtooth and slitted trailing edge geometries, Proc. 20th Int. Congr. Acoust. ICA 10 (2010) 1–9.

[19] S. C. Schlanderer, R. D. Sandberg, DNS of a Compliant Trailing-Edge Flow, in: 19th AIAA/CEAS Aeroacoustics Conf., American Institute of Aeronautics and Astronautics, Reston, Virginia, 2013, pp. 1–18.

[20] C. Das, A. Mimani, R. Porteous, C. Doolan, An experimental investigation of flow-induced noise mechanism of a flexible flat-plate trailing-edge, Annu. Conf. Aust. Acoust. Soc. 5 (2015) 1–10.

[21] E. Talboys, C. Brücker, Upstream shear-layer stabilisation via self-oscillating trailing edge flaplets, Exp. Fluids 59 (2018) 145.

[22] L. Kamps, T. F. Geyer, E. Sarradj, C. Brücker, Vortex shedding noise of a cylinder with hairy flaps, J. Sound Vib. 388 (2016) 69–84.

[23] L. Kamps, C. Brücker, T. F. Geyer, E. Sarradj, Airfoil Self Noise Reduction at Low Reynolds Numbers Using a Passive Flexible Trailing Edge, in: 23rd AIAA/CEAS Aeroacoustics Conf., June, American Institute of Aeronautics and Astronautics, Reston, Virginia, 2017, pp. 1–10.

[24] T. F. Geyer, L. Kamps, E. Sarradj, C. Brücker, Vortex Shedding and Modal Behavior of a Circular Cylinder Equipped with Flexible Flaps, Acta Acust. united with Acust. 105 (2019) 210–219.

[25] E. Talboys, T. F. Geyer, C. Brücker, An aeroacoustic investigation into the effect of self-oscillating trailing edge flaplets, J. Fluids Struct. (2019) 1–13.

[26] E. Talboys, T. F. Geyer, C. Brücker, Influence of self-oscillating trailing edge flaplets on turbulent boundary layer trailing edge noise ., in: 23rd Int. Congr. Acoust., Aachen.

[27] E. Sarradj, C. Fritzsche, T. F. Geyer, J. Giesler, Acoustic and aerodynamic design and characterization of a small-scale aeroacoustic wind tunnel, Appl. Acoust. 70 (2009) 1073–1080.

[28] E. Sarradj, A fast ray casting method for sound refraction at shear layers, Int. J. Aeroacoustics 16 (2017) 65–77.

[29] P. Welch, The use of fast Fourier transform for the estimation of power spectra: A method based on time averaging over short, modified periodograms, IEEE Trans. Audio Electroacoust. 15 (1967) 70–73.

[30] T. F. Brooks, W. M. Humphreys, A deconvolution approach for the mapping of acoustic sources (DAMAS) determined from phased microphone arrays, J. Sound Vib. 294 (2006) 856–879.

[31] Z. Xin, Y.-B. Liu, P. Chen, F. Shen, S.-J. Zhang, X.-R. Fu, Flutter frequency based on bending - torsion coupling theory, in: 8th Int. Conf. Comput. Methods, Guilin, Guangxi, China.

[32] M. S. Howe, Trailing edge noise at low mach numbers, Journal of Sound and Vibration 225 (1999) 211–238.

[33] H. Yu, Z. Yang, A Numerical Simulation on the Airfoil S833 Equipped with Flapping Trailing Edge Fringes, J. Appl. Fluid Mech. 13 (2020) 571–582.

[34] N. Simiriotis, G. Jodin, A. Marouf, P. Elyakime, Y. Hoarau, J. Hunt, J. Rouchon, M. Braza, Morphing of a supercritical wing by means of trailing edge deformation and vibration at high Reynolds numbers: Experimental and numerical investigation, J. Fluids Struct. 91 (2019) 102676.